2013-04-25

Reconfigurable Fiducial-Integrated Modular Needle Driver For MRI-Guided Percutaneous Interventions

Wenzhi Ji
Worcester Polytechnic Institute

RECONFIGURABLE FIDUCIAL-INTEGRATED MODULAR NEEDLE DRIVER FOR MRI-GUIDED PERCUTANEOUS INTERVENTIONS

by

Wenzhi Ji

A Thesis

Submitted to the Faculty

of the

WORCESTER POLYTECHNIC INSTITUTE

in partial fulfillment of the requirements for the

Degree of Master of Science

In

Biomedical Engineering

by

_____

May 2013

APPROVED:

Professor Gregory S. Fischer, Major Advisor

Professor Glenn R. Gaudette, Committee member

Professor Stephen S. Nestinger, Committee member

Abstract

Needle-based interventions are pervasive in Minimally Invasive Surgery (MIS), and are often used in a number of diagnostic and therapeutic procedures, including biopsy and brachytherapy seed placement. Magnetic Resonance Imaging (MRI) which can provide high quality, real time and high soft tissue contrast imaging, is an ideal guidance tool for image-guided therapy (IGT). Therefore, a MRI-guided needle-based surgical robot proves to have great potential in the application of percutaneous interventions. Presented here is the design of reconfigurable fiducial-integrated modular needle driver for MRI-guided percutaneous interventions. Further, an MRI-compatible hardware control system has been developed and enhanced to drive piezoelectric ultrasonic motors for a previously developed base robot designed to support the modular needle driver. A further contribution is the development of a fiber optic sensing system to detect robot position and joint limits. A transformer printed circuit board (PCB) and an interface board with integrated fiber optic limit sensing have been developed and tested to integrate the robot with the piezoelectric actuator control system designed by AIM Lab for closed loop control of ultrasonic Shinsei motors. A series of experiments were performed to evaluate the feasibility and accuracy of the modular needle driver. Bench top tests were conducted to validate the transformer board, fiber optic limit sensing and interface board in a lab environment. Finally, the whole robot control system was tested inside the MRI room to evaluate its MRI compatibility and stability.

Acknowledgements

I would first like to express my sincerest gratitude to my advisor, Dr. Gregory Fischer, for all the support and guidance from the onset of my experience at Worcester Polytechnic Institute. He has fund of knowledge in medical robotics and gives me more instruction in electronic circuit design. His technical expertise and visionary leadership has significantly guided my research work and career development. I attribute the level of my master degree to his encouragement and effort and without him in this thesis, too, would not have been completed or written.

Besides my advisor, I would like to thank the rest of my thesis committee: Prof. Glenn R. Gaudette and Prof. Stephen S. Nestinger, for their encouragement and insightful comments.

Furthermore, I would also like to express my deepest gratitude to my fellow labmates in Automation and Interventional Medicine Lab. Wenjian Shang gave me more basic knowledge of circuit design and PCB design. Gang Li helped me a lot with the software and mechanical design. Alex Camilo gave me more help with motor driving system. In addition, I will also thank Hao Su, Yunzhao Ma, Hanling Hong and Guangda Lu for their numerous help both in academic and in life.

Finally, I would like to thank my parents, Anzhong Ji and Yuhong Lu, for supporting me throughout all my studies at Worcester Polytechnic Institute. I would especially like to thank them for their encouragement and understanding when I am in troubles in both in master study and life. Their selfless love from another side of the world always keeps me moving forward.

Dedication

This thesis is dedicated to my parents Anzhong Ji and Yuhong Lu.

Contents

List of Figures

List of Tables

1. Overview

1.1Background on Image-guided Surgery

Image-guided surgery (IGS) has become a hot topic in recent medical device development and is becoming more and more widely adopted by surgeons. To date, a variety of robotic devices for image-guided interventional procedures have been developed [1-4]. With the development of modern imaging technology such as magnetic resonance imaging (MRI), computed tomography (CT) and ultrasound (US) imaging, IGS provides the surgeon more information about the operation at surgical site. IGS also improves the operating precision for the surgeon, particularly crucial for minimally invasive surgery (MIS). The patients can benefit a lot because of less discomfort, shorter healing time and reduced risk of complications. Currently, a typical IGS procedure has the following five step processes for IGS [5]:

1) Collect preoperative tomographic images from medical imaging equipment
2) Localize and track the position of the therapeutic robot or surgical tool
3) Register the localizer to the coordinate system of patient
4) Display the position of therapeutic robot or instrument in the collected preoperative data
5) Explain differences between the preoperative data and the intraoperative reality.

IGS has been developed for more than 20 years. There are a number of imaging systems which can be utilized for IGS. CT scanning, also known as computed axial tomography (CAT) scanning, is a medical imaging procedure that uses x-rays to show cross-sectional images of the body. This imaging is commonly used for bones, lung and chest. Wang.et al. developed a hybrid robot system guided by CT for percutaneous lung cancer cryosurgery [6]. The detailed structure is analyzed based on screw theory and the displacement manifold

which has 9 degrees of freedom (DOF) is shown in Fig. 1.1. Ultrasound imaging utilizes high-frequency sound to image internal structures with the differing reflection signals produced when a beam of sound waves is projected into the body and bounces back at interfaces between those structures. Kim.et al. demonstrated a new robot for manipulating a transrectal ultrasound probe for image-guided prostate intervention [7]. The robot positions and orients the probe for image scanning and targeting of the prostate. It includes 4 DOF that are available in manual handling of the probe shown in Fig. 1.2.

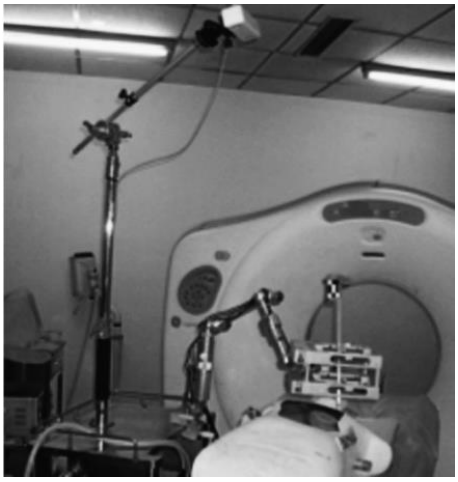

Figure 1. 1: A CT-guided hybrid robot system for lung cancer percutaneous intervention [6]

Figure 1. 2: A robot for manipulating a transrectal ultrasound probe for image-guided prostate intervention [7]

MRI provides information that differs from other imaging modalities, which can characterize and discriminate among body tissues using their physical and biochemical properties such as water, iron, fat and extravascular blood. It provides high contrast between the difference soft tissues of the body, which makes it especially useful in imaging the brain, muscles, the heart, and cancers compared with other medical imaging technology. MRI contrast agents can also be injected intravenously to enhance the appearance of blood vessels, tumors or inflammation. However, the MR image has some other disadvantages. The MR image has high cost when compared to the other imaging system. In addition, the MRI-guided medical device should be nonmagnetic, which has a high requirement for the materials.

Such advantages of MRI have made it rapidly developing in image-guided surgical interventions. Krieger.et al. at Johns Hopkins University presented a novel remotely actuated manipulator for access to prostate tissue under MRI device guidance, designed for use in a standard high-field MRI scanner [8]. Fig. 1.3 shows that this device provides 3D MRI guided needle placement with millimeter accuracy under physician control. After eight year, this team demonstrated another MRI-guided robotic system with accuracy sufficient for targeting clinically prostate cancer [9]. Fig. 1.4 shows the new generation of the actuated robot mechanical design.

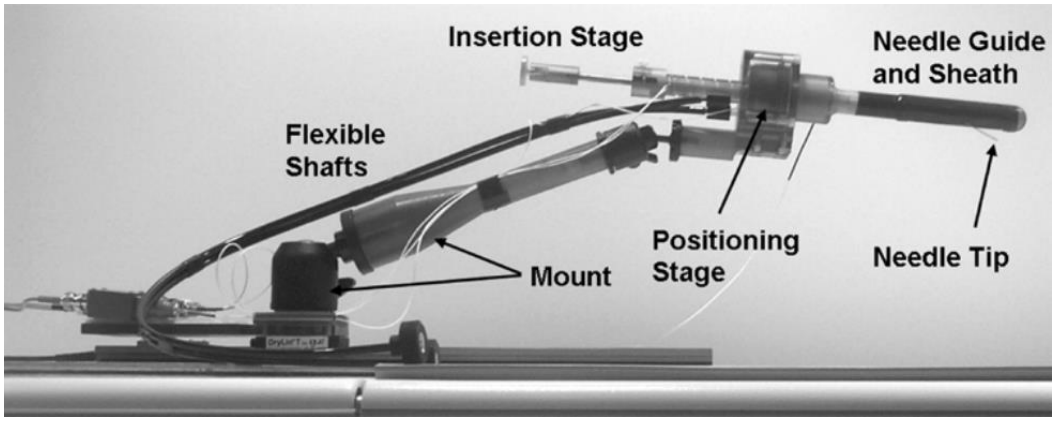

Figure 1. 3: A remotely manually actuated manipulator for access to prostate tissue under MRI guidance [8]

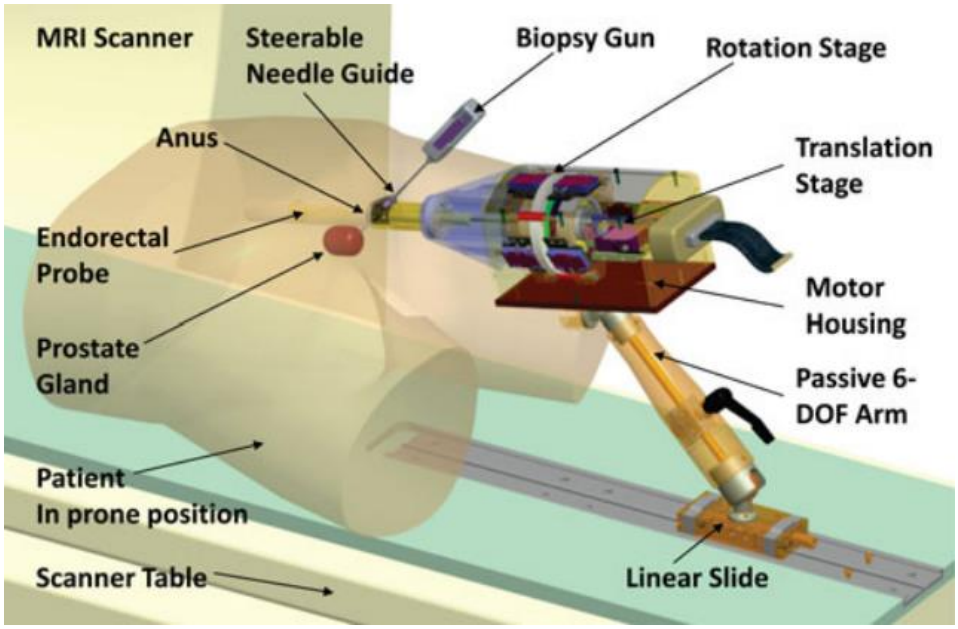

Figure 1. 4: A new generation actuated MRI-Guided robotic system for prostate intervention [9]

Western University presented a device that has been developed for delivering prostate focal thermal therapy under MRI guidance [10]. The significant feature is capable of delivering needles to targets in the prostate without removing the patient from the scanner, which

greatly reduces procedure time and increases accuracy. The mechanical design is shown in Fig. 1.5.

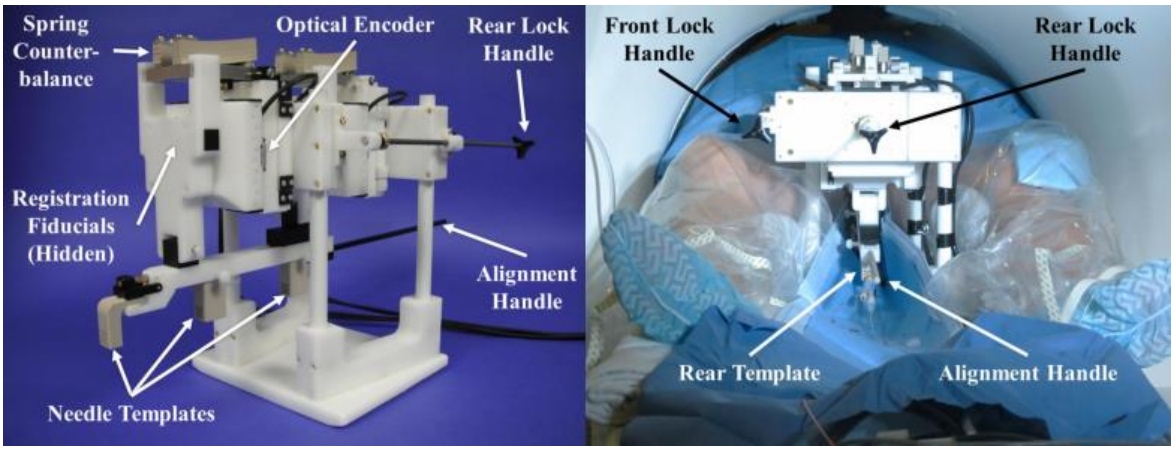

Figure 1. 5: A MRI-guided device for delivering prostate focal thermal therapy [10]

Fischer et al. at Johns Hopkins University demonstrated a prototype of an MRI-compatible manipulator and the support system architecture that can be used for needle placement in the prostate for biopsy and brachytherapy procedures [11]. Fig. 1.6 shows the detailed mechanical design of the pneumatically actuated robot.

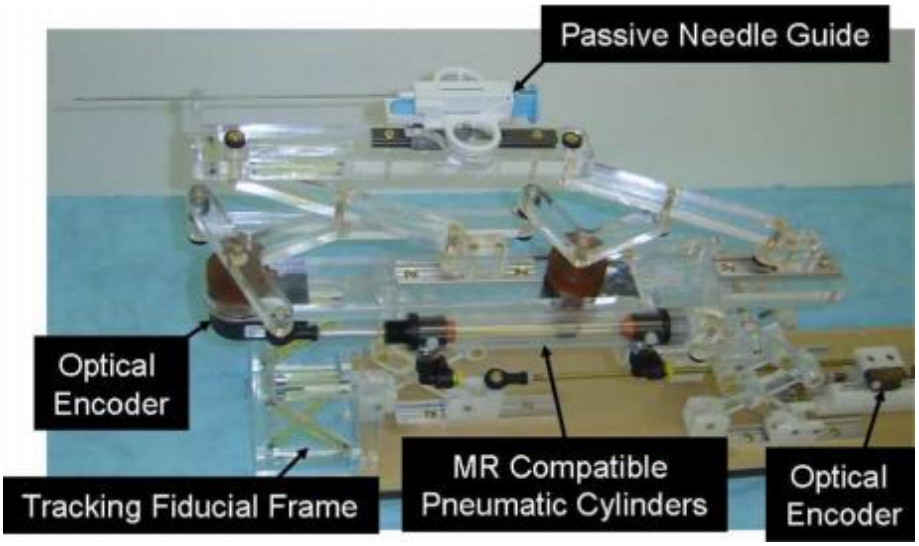

Figure 1. 6: A prototype of an MRI-compatible manipulator [11]

1.2 Background on Needle-Based Interventions

To date, needle-based interventions have become more and more popular in frontier research areas of surgical interventions. Needle-based interventions are pervasive treatments in Minimally Invasive Surgery (MIS) and different combination of needle, tube can be applied in a great number of diagnostic and therapeutic procedures, including biopsy tissue sample retrieval and brachytherapy seed placement.

Biopsy is a medical test commonly performed by a surgeon taking sampling of cells or tissues, which can be examined under a microscope or analyzed chemically. This surgical procedure can also be accomplished by automatic mechanism. Haytham.et al. presented a robotic system to perform transrectal prostate biopsy inside a 1.5-T closed bore MRI scanner [12]. The robot manipulator consists of 5 DOF in Fig. 1.7, with 3-DOF Cartesian stage and 2-DOF biopsy needle insertion and firing mechanism. Another new workspace-optimized 4-DOF parallel robot was developed by Song for the MRI-guided prostate biopsy [13] shown in Fig. 1.8.

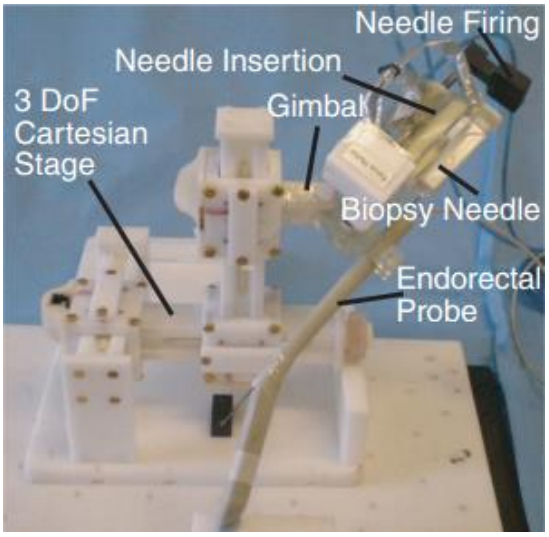

Figure 1. 7: A 5-DOF transrectal prostate biopsy [12]

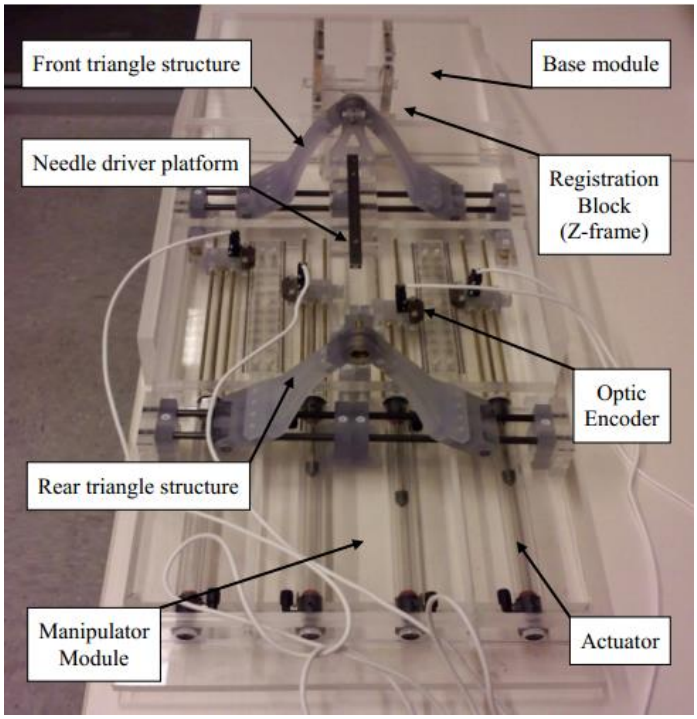

Figure 1. 8: Workspace-optimized 4-DOF parallel robot for prostate biopsy [13]

One specific procedure [14] of clinical targeting of a biopsy needle is shown in Fig. 1.9:

1) Align the robot to the plane of the entry point
2) Insert the cannula to the depth of L before the target position, guaranteeing the sample at the center of notch.
3) Insert stylet distance of 2L, making the notch center at target sample position.
4) Perform coordinated motion to insert cannula and retract stylet with the same length 2L and under the same speed to capture the sample inside the needle.
5) Retract needle containing the biopsy core to home position.

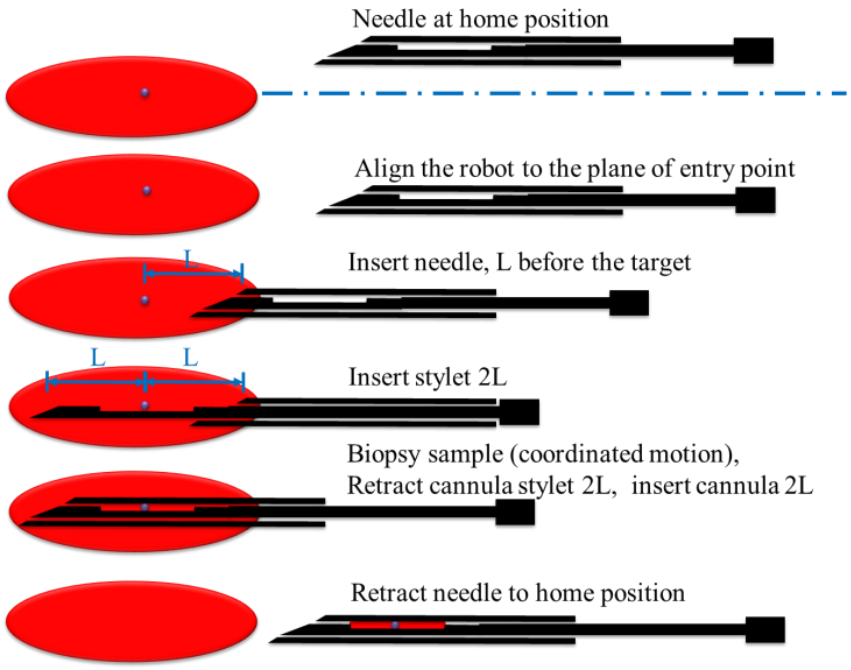

Figure 1. 9: The clinical procedure for executing automated biopsy [14]

Brachytherapy is a form of radiotherapy where seeds are placed in a complex distribution inside or near the area requirement treatment, which is commonly used as an effective treatment for cervical, prostate, breast, and skin cancer and can also be used to treat tumors. In 2006, Yan.et al. developed and fabricated a 16 DOF robotic system for prostate brachytherapy, with 9 DOF positioning module and 7 DOF surgery module [15] shown in Fig. 1.10. Fichtinger .et al. demonstrated an image-guided robotic system for accurate and consistent placement of transperineal needles into the prostate with intraoperative image guidance inside the gantry of a computed tomographic scanner [16] shown in Fig. 1.11.

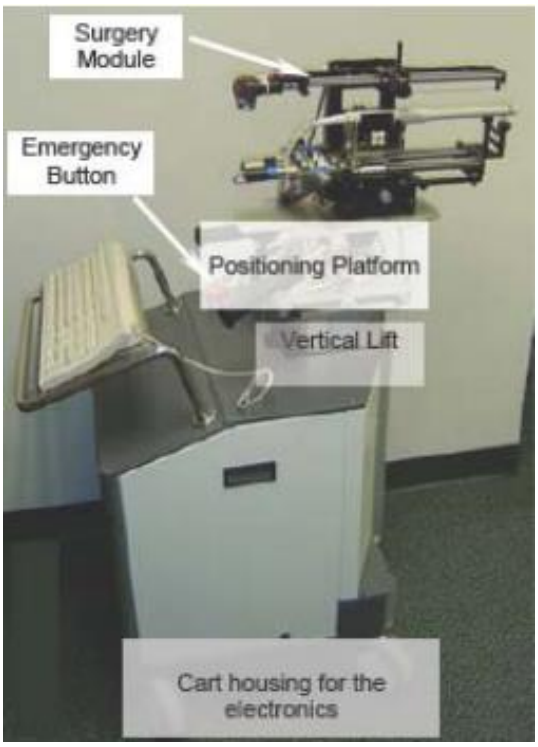

Figure 1. 10: A 16-DOF system for prostate brachytherapy [15]

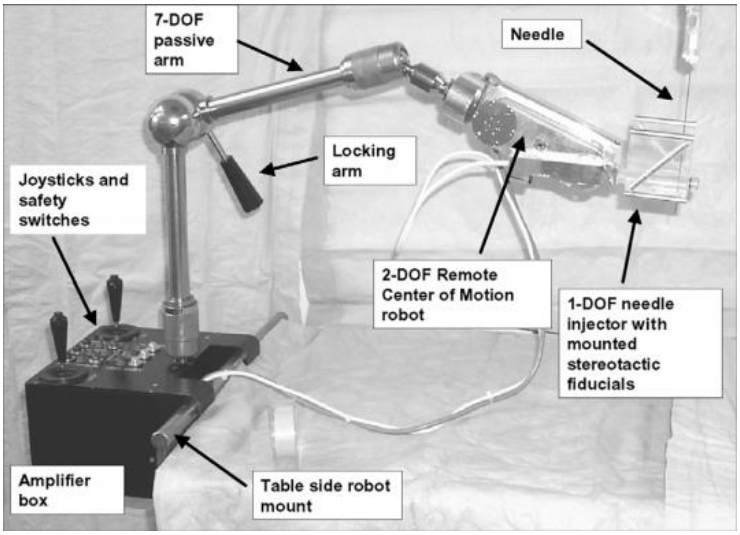

Figure 1. 11: A CT-Guided transperineal needle for prostate brachytherapy [16]

One specific procedure [14] for executing brachytherapy based on pre-loaded needles (a commonly used approach) is shown in Fig. 1.12 and can be specified in the unified workflow:

1) Retract stylet joint to depth L, and load the seeds and spacers to the brachytherapy needle according to the treatment plan. (L equals to the sum of the length of the seeds and the spacers.) Alternatively, pre-loaded needles may be loaded into the needle driver.
2) Align the robot such that the needle axis is in line with the planned entry point.
3) Insert the cannula along the needle axis to the target position.
4) Deliver seeds under automatically coordinated motion, retracting cannula and inserting stylet with the same length L and under the same speed.
5) Retract needle to home position.

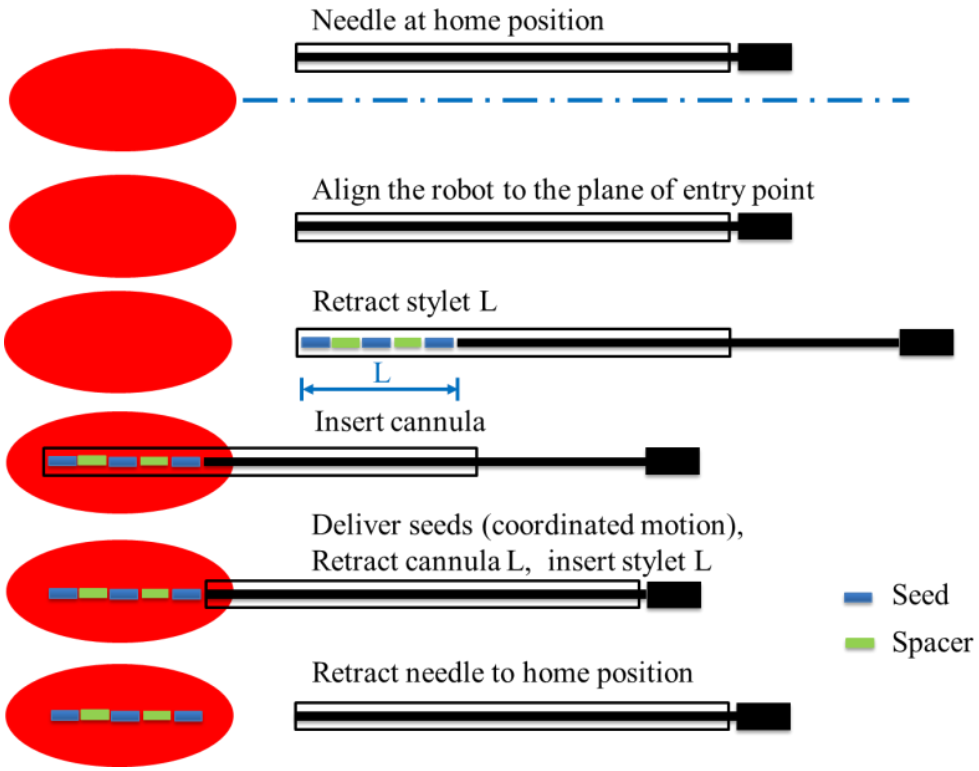

Figure 1. 12: The clinical procedure for executing automated brachytherapy seed delivery [14]

In addition, the needle-based intervention also has other diagnostic and therapeutic procedures, such as delivery of therapeutic agents and thermal therapy. These also are the reasons that why needle-based surgical interventions are such popular in the frontier research area.

1.3 Thesis Contribution

As described previously, various kinds of MRI compatible surgical robots have been developed in recent years. Generally, these surgical robots are needle-based and guided by MRI to implement prostate interventions. However, to date, there are few surgical needle drivers featuring modularity and compact design. Most of these mechanical designs presented above are not flexible to enable more complex controlled motion profiles for percutaneous interventions, such as biopsy and brachytherapy. In addition, it is also uncomfortable for the patients if the needle driver occupies too much volume.

The thesis strives to design and evaluate an MRI-guided and needle-based surgical robot system for percutaneous interventions. The primary contributions focused on developing a modular robotic needle driver device and the corresponding electrical control system. As such, the specific major contributions are listed as following:

1) Developed and evaluated a compact, reconfigurable MRI-compatible needle driver, using modular design approach, to support various needle-based percutaneous interventions. A compact cylindrical helix imaging coordinate registration fiducial frame was integrated in this needle driver such that its axis is concentric with needle base. The integration enables the real-time MRI-guided percutaneous interventions with high precision and compact size.

2) Further developed and refined a controller for closed loop control of the piezoelectric ultrasonic Shinsei motor which is integrated into the independently developed base robot that supports the needle driver developed in this work. The study presented a custom transformer PCB to cooperate with the previously developed MRI robot controller piezoboard so as to enable use of the high power Shinsei motors. In addition, this work also developed an interface PCB board to provide the base robot with eight-channel fiber optic limit switches, four Shinsei motor and encoder connectors and four external encoder connectors. Furthermore, both the transformer board and interface board were tested and evaluated.

1.4 Thesis Organization

The thesis is composed of three main parts including the design and evaluation of needle driver, transformer board and interface board.

Chapter 2 presents and evaluates a reconfigurable fiducial-integrated modular needle driver for MRI-guided percutaneous intervention. The motivation and goal is introduced at the beginning of this chapter. Then the requirement and system architecture are described. Further, the needle driver is presented in terms of mechanical design, cylindrical fiducial integration and MRI compatible components selection. Finally, a bench top test is carried out for evaluating the feasibility and accuracy of the system.

Chapter 3 demonstrates a controller system for ultrasonic Shinsei motors that are integrated in the base robot that supports the needle driver developed as part of this work. An ultrasonic Shinsei motor is introduced including mechanical structure, schematic, characteristics and specification. A waveform synthesizer is presented to generate the four phases of the drive signals for piezoelectric motor. Then a transformer board is designed and manufactured for

interfacing ultrasonic Shinsei motors with the MRI robot control system. A bench top test is presented to demonstrate its feasibility and stability.

Chapter 4 demonstrates an interface board for connecting controller box and surgical robot, ensuring the safety of the base robot. The motivation and goals are discussed and electronic components selection is presented. Then the optical limit switch circuit is designed. Finally, a interface board is designed using Altium Designer software and a bench top test is conducted in lab environment.

Chapter 5 summarizes the contribution of the work, evaluation results, and conclusion with suggestion of future work.

2. Development of Reconfigurable Fiducial-Integrated Modular Needle Driver for MRI-Guided Percutaneous Interventions

2.1 Motivation and Goals

Prostate cancer is the most common cancer in the United States. According to statistics of the America Cancer Society, about 1 man in 6 will be diagnosed with prostate cancer during their lifetime. In addition, older men tend to suffer from prostate cancer. Nearly two thirds are diagnosed as prostate cancer in men aged 65 or older. The fact that 1 man in 36 will die of prostate cancer makes it to be the second leading cause of cancer death in the United States, just following lung cancer [17]. To date, needle biopsy and brachytherapy are the commonly used diagnosis method and treatment method for prostate cancer.

The Automation and Interventional Medicine (AIM) Lab at WPI has developed a surgical robot for percutaneous interventions for prostate cancer diagnosis and therapy [18]. This piezoelectric robotic needle placement mechanism has 3DOF: two linear translations and one axial rotation shown in Fig.2.1. This piezoelectric approach can be used for biopsy and brachytherapy. However, this mechanical design has several disadvantages. One is that this needle driver is not modular, which cannot achieve active cannula in complex tissue system. Another is that the dimension of this design occupies more space, which is not convenient in MRI-Guided surgery. Therefore, we try to design a compact, reconfigurable MRI-compatible needle driver, using modular design approach, to support various needle-based interventions

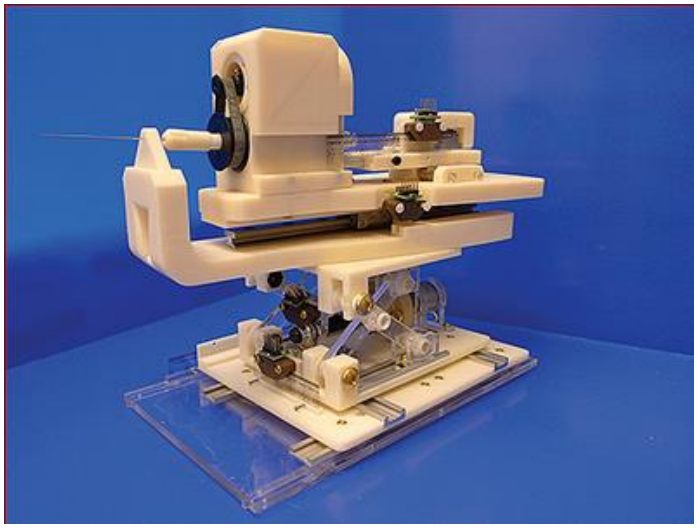

Figure 2. 1: Physical prototype of 6-DOF piezoelectric needle placement robot for prostate intervention

2.2 Requirement

The significant function of this needle driver is to achieve transperineal needle deployment in patient suffered from prostate cancer for diagnosis and treatment, mainly by the form of biopsy and brachytherapy. In MRI room, the patient is placed in the supine position with the legs side open and uplifted as shown in Fig.2.2. The prostate medical robot will operate in the limited space between the patient's legs without inference with patient and MRI scanner machine. From the Fig.2.2, we can recognize that the sizes of width and height are confined due to the structure of human beings. However, the size of length seems to be sufficient making modular design possible. Therefore, the needle driver should reduce the width and height as much as possible. Generally, the proper size of medical robot for prostate interventions could be 1000x150x150mm.

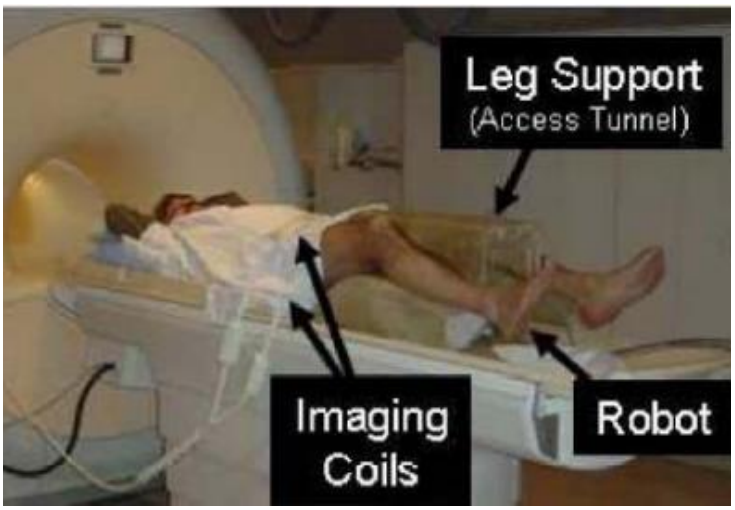

Figure 2. 2: Prostate surgery inside the MR room [18]

The average size of prostate is 50mm in the lateral direction by 35mm in the anterior-posterior direction by 40mm in length. To cover all volume of prostate, the prostate can be assumed to be a sphere with 50mm diameter. We can estimate the requirement for insertion depth is 100mm. The rotation degree should be 360 degrees.

The system requirement is achieving modularity and 2 DOF for each separate module. Modularity is the degree to which a system's components may be separated and recombined. The needle driver will have more concentric needles, tubes, and cannula in order to achieve more complex and changeable needle placement for different surgical interventions. The needle driver consists of multiple actuation units, which are necessary identical independence. In addition, each individual actuation unit should have 2 degrees of freedom – 1 DOF linear translation and 1 DOF axial rotation.

An imaging coordinate registration fiducial frame is required to be integrated to this new needle driver. Because this prostate surgery belongs to minimally invasive surgeries, the needles or tubes will be inserted or placed in to human body. It is obvious that accurate and

effective administering of the deployment heavily contributes to efficiency of these treatments. Also, precise and effective image guided methods are required to ensure the accurate delivery of radioactive seed for treatment of prostate cancer.

Another requirement is the MRI compatible design. This intervention is designed for MRI-guided prostate surgery, which means that this needle driver system will operate inside the area with 1.5 – 3T magnetic field. Therefore, traditional mechanical materials, sensor and actuators cannot be employed in this design. No ferrous materials are allowed in this system.

2.3 System Description

The mechanism is capable of positioning a needle to perform diagnosis by taking tissue samples inside the prostate or early treatment by placing radioactive seeds inside the tissue, remotely controlled by the physician without moving the patients out the of the MRI imaging area. The needle driver enables real-time MRI-guided operation for precise placement of needles in real soft tissue.

A compact cylindrical helix imaging coordinate registration fiducial frame designed and integrated in this needle driver can help place shaped tubular surgical tools accurately in the MRI-guided medical surgical interventions. This registration fiducial frame plays an important role in registering the prostate medical robot to the patient coordinate system in the MRI working space.

Modular design is also a significant concept in medical design. In the mechanical design, each actuation unit can support one needle, tube or cannula. Several actuation units mean that several needles, tubes and cannulas can be assembled together to form different kinds of needle shapes. More similar modules will succeed in achieving more complex controlled

motion for biopsy, brachytherapy, and concentric-tube needle deployment, such as active cannula, which can realize “s” curve to avoid the crucial tissue parts inside the patients shown in Fig.2.3. This “s” shape needle consists of three tubes and each tube is pre-curved. The needle driver has enough space for more similar modules by modifying the length of lead screw and linear guide.

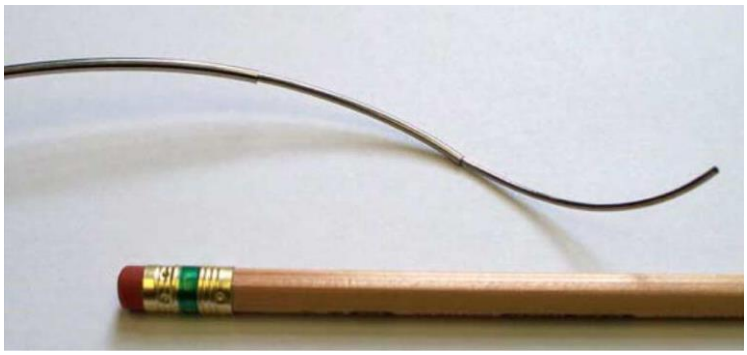

Figure 2. 3: Active cannula composed of three telescoping Nitinol tubes, which is actuated by rotating and translating the tubes at their bases [45]

2.4 Mechanical Design

2.4.1 Mechanical Design of Needle Driver Modular

A modular design approach is utilized in the design of the needle driver to enable universal and multipurpose needle intervention. The new designed needle driver will be placed on top of existing base platform Cartesian stage described in Fig.2.4. This Cartesian stage previously designed by AIM lab has 3 DOF including X, Y and Z.

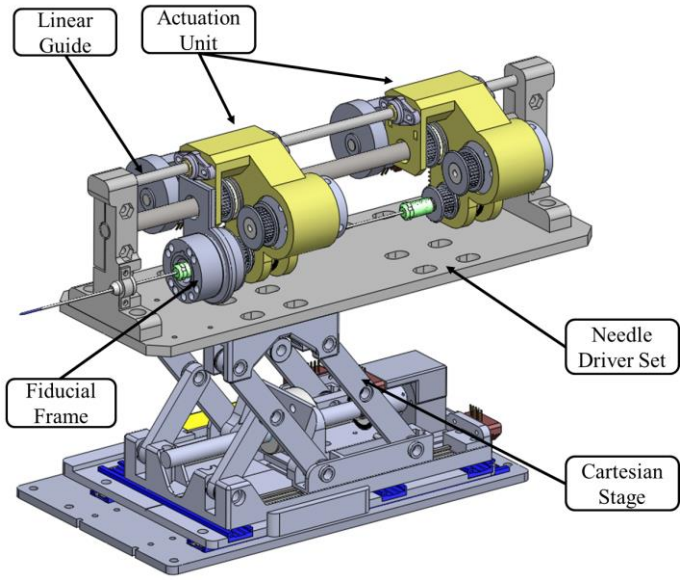

Figure 2. 4: CAD model of the needle driver set shown in an exemplary configuration of two 2-DOF modules, mounted on a Cartesian stage. The driver may be configured for additional modules with various lengths of travel depending on the application, and be mounted to various base platforms.

The most important feature of this needle driver is modularity. The design consists of multiple actuation units, essentially identical and independent, decoupled motion, as shown in Fig.2.4. The needle driver can be lengthened or shortened according to complex controlled motion profiles for biopsy, brachytherapy, and concentric-tube needle deployment, by adjusting the length of lead screw and linear guide. In this design, two modular units are assembled and evaluated. Each individual actuation unit can drive a single needle, tube, or cannula, and has 2 degrees of freedom (DOF) motion, with 1 DOF linear translation and 1 DOF axial rotation. Each mount house rides on a common aluminum lead screw and linear guide which is firmly fixed on the based robot mechanism. The nut is rotated using a timing belt drive mechanism. The motor rotates nut through the pulley sets and the whole modular unit moves along the lead screw, achieving 1 DOF linear translation. Actually, the lead screw and linear guide are fixed on the base stage. The needle clamping mechanism is attached to a

pulley which is driven by similar timing belt drive mechanism. The motor also rotates the collet clamping mechanism through the pulley set, enabling 1 DOF axial rotation.

The needle has different type and ranging size. They are clamped by a universal collet supporting different sizes of standard needles from 25 Gauge (0.51mm) to 16 Gauge (1.65mm). The specific size of the needle should be based on different applications. A sterile sleeve needle is used to ensure sterility of all needle-contacting components.

The center distance between the tube clamping and motor ranging will have effect on the accuracy of mechanism. An eccentric belt tensioner is designed to adjust the center distance between the tube clamping and motor shown in Fig.2.5. This design will ensure the effective and smooth power transmission via twisting the motor mount house to varying house angles with respect to the tube clamping mechanism [19].

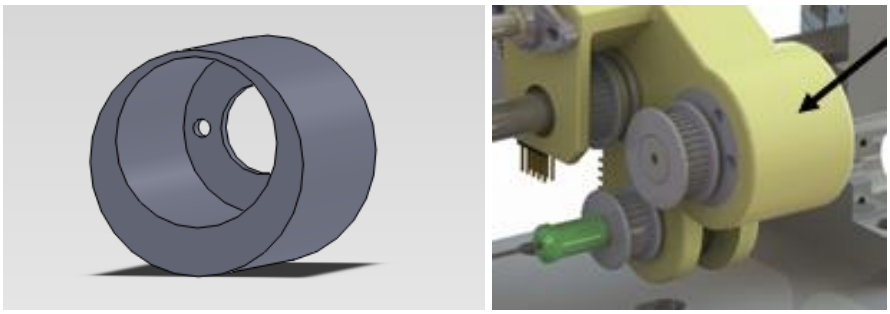

Figure 2. 5: Eccentric motor mount design

For the translation actuator, the transmission pulley is further far away from eccentric belt tensioner, also clipped an optical encoder strip during intermediate position. This will possibly result in curving pulley, bringing about abnormal working of the optical encoder. In this design, two fixed parts were extended from itself eccentric belt tensioner to adjust the bent of motor pulley.

Exploded view of the actuation unit is shown in Fig.2.6.

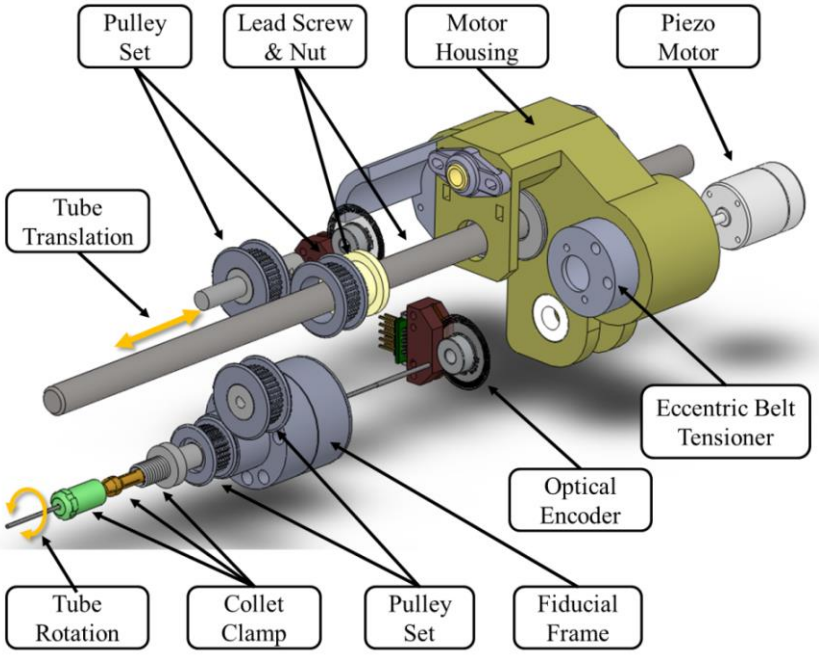

Figure 2. 6: Exploded view of a 2-DOF actuation unit module

2.4.2 Fiducial Frame Integration

2.4.2.1 Review

In last decade, the tubular shaped surgical tools, such as needles, tubes, shunts and drills, are often used for surgical intervention in many minimally invasive surgeries. A number of physical delivery therapies to the tumor have presented for a stereotactic problem such as prostate intervention [19] and deep brain stimulation [20]. Therefore, more effective methods are needed to ensure the accuracy delivery of therapy. To date, MRI guided technique has a widely application in tumor surgical intervention, for its high soft-tissue contrast image [21]. Therefore, knowing the position and orientation of surgical robot related to the patients is a key factor in percutaneous interventions. The imaging coordinate registration fiducal frame is designed for this particular application.

To date, a number of registration and tracking approaches have been talked including active coils, encoders and passive fiducials [22]. Some active tracking coils have been discussed by Krieger [22], Derbyshire [23] and Hillenbrand [24]. This active tracking method has the advantage of high accuracy and tracking speed. However, it also accompanies with several disadvantages such as special scanner programming, limitations of scanner channel and special design of electronic hardware [22]. DiMaio and Susil have discussed both passive single-image registration and tracking in MRI and CT environment [25,26]. Lee has designed several numerical algorithms to make the single image registration more accurate [27]. In addition, high accuracy muti-image registration approaches have been developed using a similar fiducial frame by Shang [28]. According to these researches, the passive fiducial does not require complicated equipment and imaging protocols compared to active tracking coils.

2.4.2.2 CHIC Fiducial

A new cylindrical helix imaging coordinate (CHIC) registration fiducial frame, based on work of Ma.et al. in the AIM Lab, is integrated into the needle driver in order to register the medical robot to the patient coordinate system in MR image space [29]. The cylindrical helix imaging coordinate fiducial frame is shown in Fig.2.7.

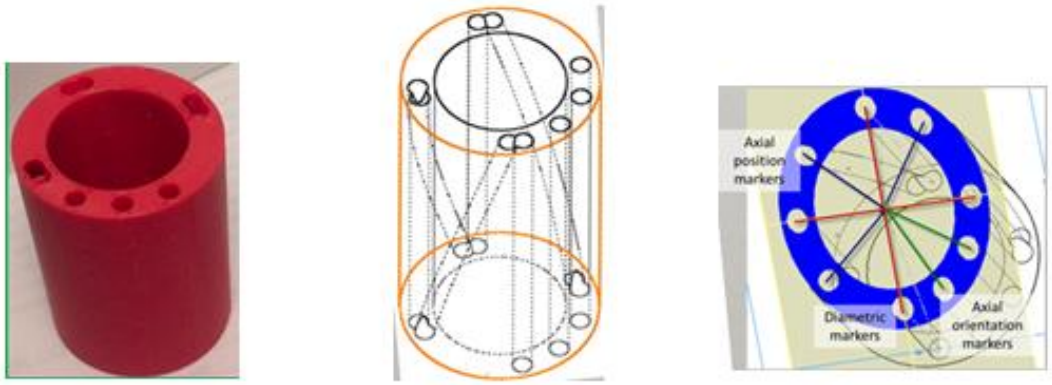

Figure 2. 7: Cylindrical helix imaging coordinate fiducial frame developed by Ma.et al. [29]

There are 9 tubes going through the whole fiducial frame design. Four straight tubes work as diametric markers to form a cruciate fiducial. Three sets of helix curves work as axis position markers to provide depth information. The final two straight tubes work to make the frame asymmetric for detecting twist angle and improving ellipse fitting [29].

The general principle is shown in Fig.2.8. In a single cross-section MRI image, there are nine points which represent nine fiducial tubes. As we know from its geometric property, these nine points should be on an ellipse. Firstly, a least square ellipse fitting is done by using those nine points. By fitting a general ellipse in the image coordinate, center position and azimuth angle could be known. The elevation angle can be estimated based on the radio of minor and major axis of ellipse. Until now, we can get 4 out of 6 DOF. The rest of 2 DOF are depth z and twist angle. To get the depth position, we first transform oriented or image coordinates to fiducial major coordinate. The twist angle is defined as the rotation around the central axis. This angle is found by detecting the angular position of axial orientation markers relative to diametric markers. Using all of these, we can detect which quadrant of the coordinate system contains a pair of marker:

one axis orientation and one diametric. This provides sufficient information to establish an estimate for the amount of twist around central axis.

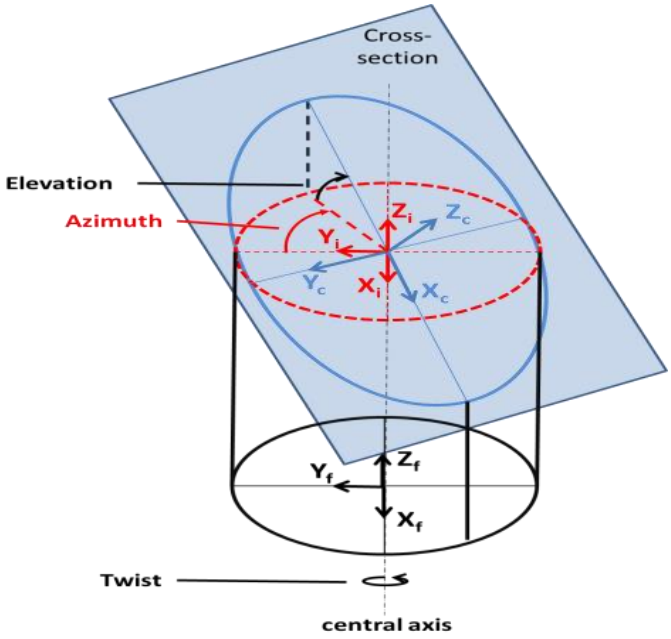

Figure 2. 8: Coordinate fiducial frame intersecting with the image [29]

This cylindrical shaped fiducial frame has a small size so that it could be easily assembled to the distal end of tubular shape surgical tools. This shaped fiducial frame also has high accuracy and high speed due to only one MRI image is needed. After evaluation, this tubular shaped fiducial frame is particularly suitable for attaching to the distal end of the needle driver, to offer direct visualization and localization from in situ MR imaging. In the needle driver design, this fiducial frame was attached concentrically with the axis of the first actuation unit in order to translate and rotate with the needle synchronously. This is shown in Fig.2.9.

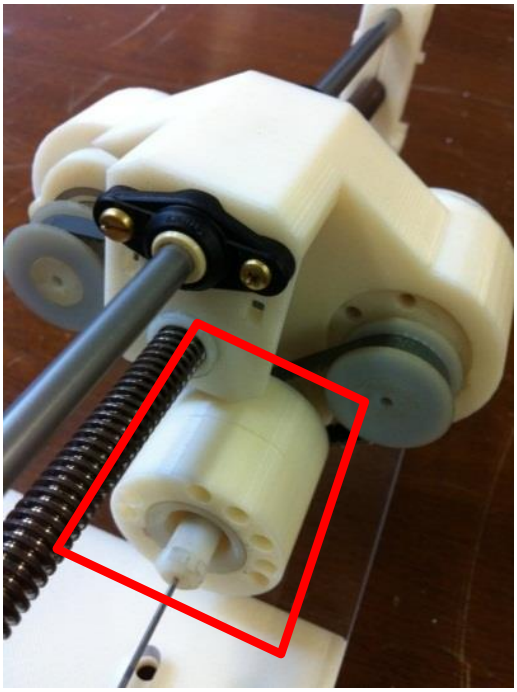

Figure 2. 9: Fiducial-integrated needle driver

2.4.3 System Component Selection

This needle driver is designed for real-time MRI-guided surgery, which requires this design to be MRI-compatible in magnetic space. Therefore, nonmagnetic materials were utilized to build the majority of the components of this needle driver. Nonconductive materials were utilized to build the majority of the components of the needle driver, non-ferrous aluminum was chosen for linear guide and lead screw, which require high stiffness, to maintain MRI compatibility.

2.4.3.1 Piezoelectric Motor

Piezoelectric motors are chosen as the actuators, for its high accuracy, dynamic performance and robustness [30]. The piezo legs rotary 80mNm motor (PiezoMotor AB, Sweden) is intended for MRI compatible intervention, as shown in Fig.2.10. This piezomotor has very high dynamics and microradian precision. In addition, high torque output in a small package

is another benefit, which making it ideal for numerous application. The piezomotor can move in full steps, short steps or partial steps with positioning resolution in the microradian range. Speed of this kind motor can be adjustable from mirco radian per second up to max speed.

Figure 2. 10: Pizeo LEGS Rotary 80mNm motor [31]

Piezo LEGS motor motion is based on the contact friction between the drive leg and the drive disc, which is different from a DC motor or stepper motor. Microstepping is achieved by dividing the waveform into discrete points. The resolution will be a combination of the resolution of the D/A converter, the number of points in the waveform, and the load. The schematic is shown in Fig.2.11. When four distinct waveforms are placed in four ceramic fingers, the ceramic fingers will generate translational motion. When all legs are electrically activated, they are elongated and bending. As we see in the figure, alternate legs move as pairs. In second stage, the first pair of legs maintains contact with the drive disc and moves towards the right. The second pair retracts and their tips begin to move left. In third stage, the second pair of legs has now extended and repositioned in contact with the drive disc. Their tips begin moving right. The first pair retracts and their tips begin to move left. In fourth stage, the second pair of legs has moved right. The first pair begins to elongate and move up towards the drive disc or strip [31].

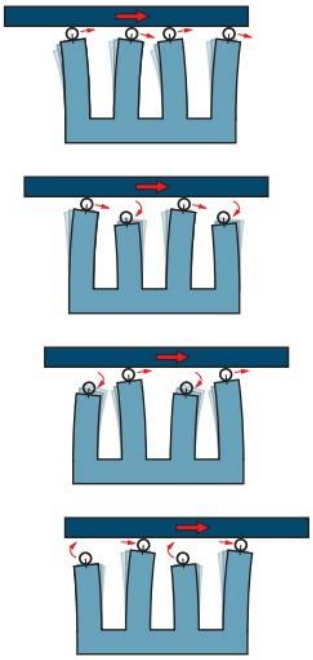

Figure 2. 11: General operating principle of piezoelectric motor [31]

The technical specification of the piezo legs rotary 80mNm motor is listed in Tab. 1.

Table 1: Technical specification for piezoelectric motor

Parameter	Data	Unit
Maximum Speed	20	RPM
Resolution	<1	Urad
Max Voltage	48	V
Stall Toque Max	80	Nmm
Holding Torque Max	90	Nmm
Material	Stainless steel	
Mechanical Size	32x23	Mm
Weight	60	Gr

2.4.3.2 Optical Encoder

The optical encoder consists of a shatterproof mylar disk mounted to a precision machined aluminum hub and an encoder module. The module consists of a highly collimated solid state light source and monolithic phased array sensor [32]. The optical encoder is a kind of photoelectric conversion sensor, which converting mechanical geometry displacement in output axis to electric pulse. This will help to record the movement distance of existed motors.

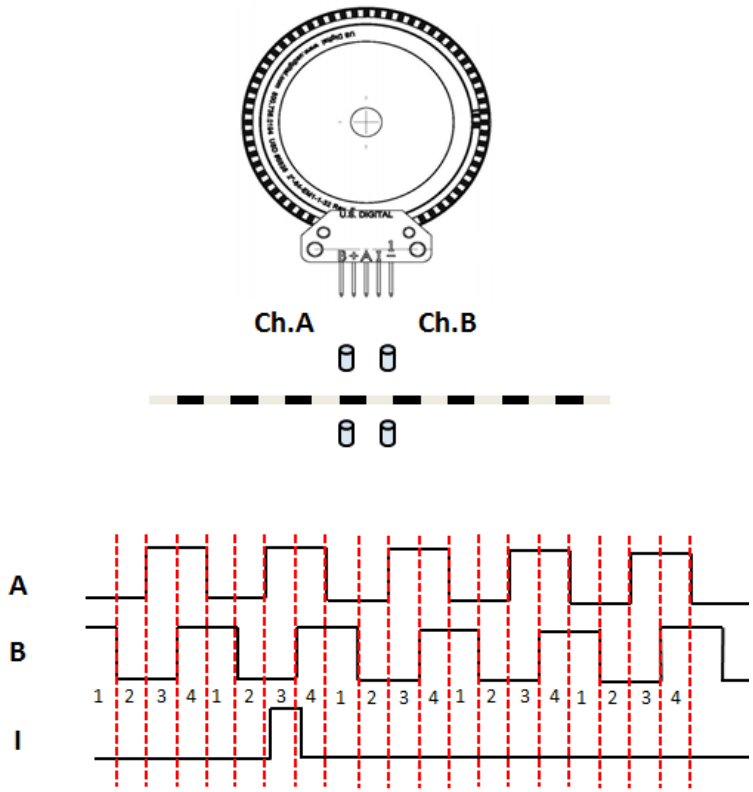

Figure 2. 12: Detailed schematic diagram of optical encoder

The optical encoder we chose belongs to incremental encoder. Its working schematic is shown in Fig.2.12. This optical encoder's disc is made of glass or plastic with transparent and opaque areas. A light source and photo detector array detects the optical pattern that results

from the disc's position at any one time. This kind optical encoder has two channels, detecting the transparent and opaque areas. We can get two channel square waves. There are four phases in each cycle period shown in Tab.2. According to the datasheet, there are 1250 opaque lines in the rotary wheel strip, with the resolution of 1250x4 lines each circle period with quadrature.

Table 2: Four phases in each cycle period for optical encoder [32]

Phase	A	B
1	0	0
2	0	1
3	1	0
4	1	1

2.4.3.3 Lead Screw guide

The needle driver will operate in MRI room, so all the components will be nonmagnetic. As is shown in Fig.2.13, the linear guide is a common aluminum shaft for supporting the whole module houses. The lead screw is an aluminum screw its size is shown in Fig.2.13. The total length is 300mm with extern diameter 10mm and pitch 2mm.

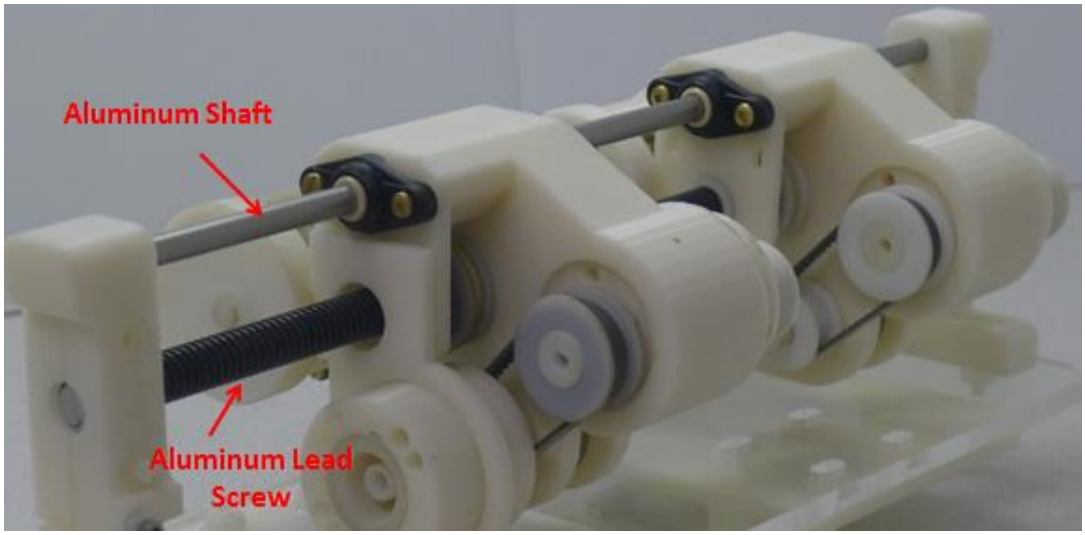

Figure 2. 13: Aluminum shaft and aluminum lead screw

2.5 Mechanism Evaluation

In this section, an experiment was designed and performed to evaluate the mechanical accuracy of this needle driver. DC motors were utilized to substitute for piezoelectric motor to drive this mechanism for mechanism testing purposes. Galil controller provides with more control access to different kinds motors and was chosen as the controller system for this needle driver.

2.5.1 Galil controller

Galil's DMC-2173 ethernet motion controllers are designed for extremely cost-sensitive and space-sensitive application. The controllers integrate a 32-bit microcontroller and provide such advanced features as PID compensation with velocity and acceleration feedforward, gram memory with multitasking for simultaneously running up to eight programs, and uncommitted I/O for synchronizing motion with external events [33].

The DMC-2173 motor controller board offers a variety of plug-in multi-axis amplifier boards that are designed to eliminate the wiring and any connectivity issues between the controller and drives. The AMP-20341 contains four linear drives for operating small brush-type servo motors. This amplifier board requires a ±12-30 DC voltage input and provides 20W per channel or 60W total output power. The AMP-20341 connects to DMC-2173 board via the 25-pin D-sub connector and offers 15-pin D-sub connectors for encoders [34]. Fig. 2.14 shows the DMC-2173 controller and AMP-20341 amplifier.

Figure 2. 14: DMC-2173 controller and AMP-20341 amplifier [34]

The galil controller uses a simple, intuitive command language which makes them very easy to program. The galiltools servo design software offers compiling environment for this command language.

2.5.2 Experiment Design

The purpose of this experiment is to evaluate system workspace verification and system accuracy.

In Fig.2.15, the test system contains galiltools, galil controller and amplifier, DC power supply, needle driver and calipers. The DC power supply provides ±12V to DMC-2173 controller board. The controller directly drives the DC motor through amplifier board. The galiltools provides compile circumstance for digital motion controller code and communicates with galil controller via ethernet. Generally, the galil controller drives the needle driver achieving linear translation and axial rotary.

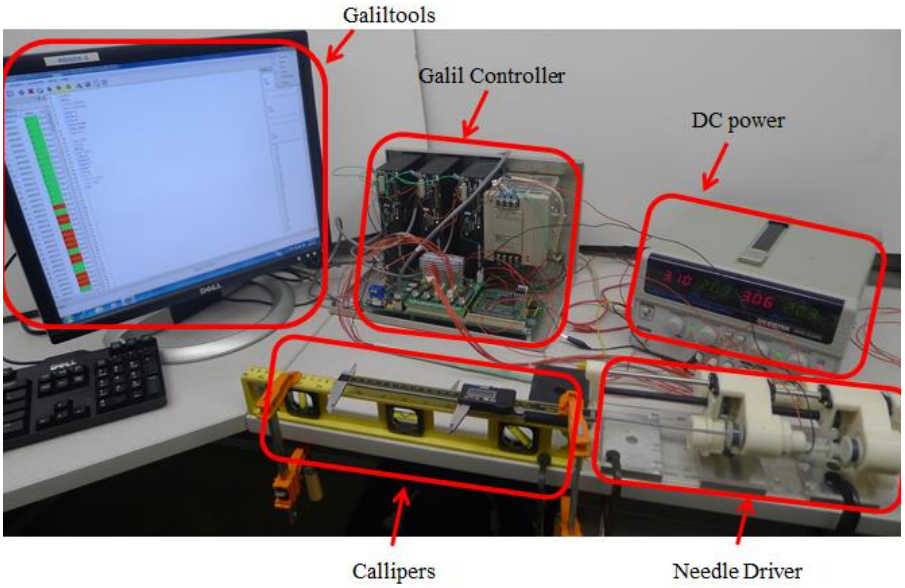

Figure 2. 15: General diagram for needle driver bench top test

Experiment I: Workspace verification

1) Used the galil controller to insert one modular needle in the whole range and rotate the axial rotary needle.
2) Used the caliper to measure the distance of whole range.

Experiment II: Accuracy evaluation

In the process of test, individual joints were set to 20 target positions driven by the robot controller

1) Each time set 8mm target position and used the Galil controller to drive the DC motor
2) Read the theoretical steps from Galiltools and calculated each step theoretical moving distance
3) Used the caliper to measure the distance of actual moving distance

2.5.3 Results

The prototype needle driver is shown in Fig.2.15 with two actuation units and a concentric tube needle. The dimension of individual actuation units are 73x116x96 mm, and the overall dimensions of the needle driver set are 300x116x96 mm. In this experiment, the needle driver can offer a 130mm linear translation and 360 degrees axial rotation for each needle or tube attached.

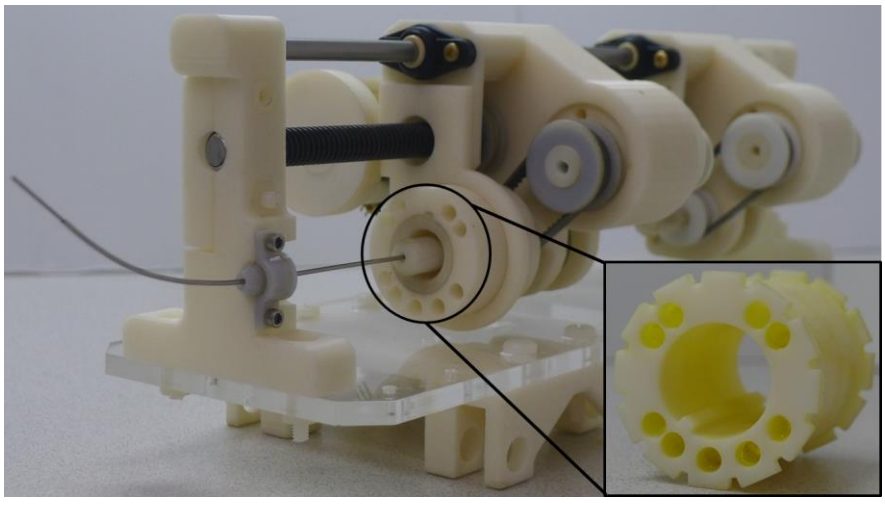

Figure 2. 16: Prototype of the needle driver set with 2 actuation units, attaching concentric-tube needles. Inset: fiducial frame filled with MR-visible gel, and CAD model of the frame showing the helix configurable concentric with the needle base

In the experiment, 20 groups of actual and target positions were recorded and the scatter plot is listed in Fig. 2.17.

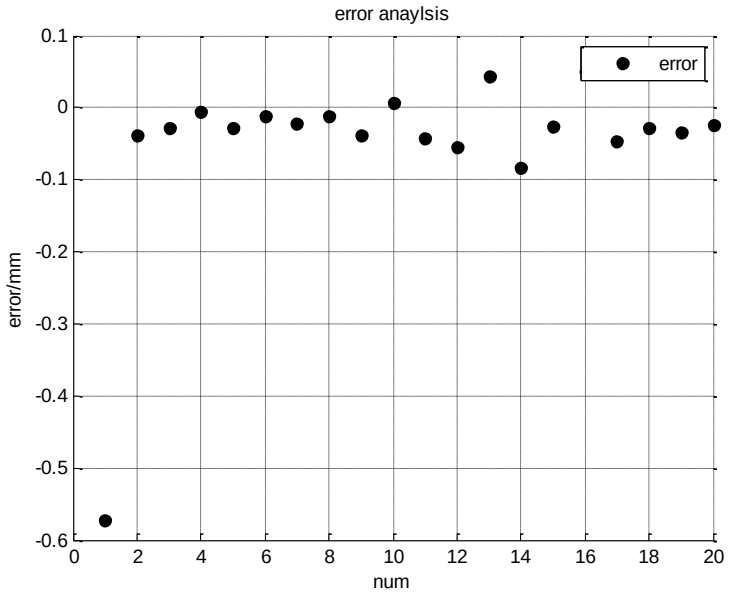

Figure 2. 17: Scatter plot of error between actual position and target position. 20 groups of actual and target positions were recorded and errors were calculated.

The RMS accuracy for the individual joints was determined to be 0.18mm with the stand deviation 0.17mm. There is no standard RMS accuracy for this kind medical design. However, many of other similar medical design have average RMS accuracy 0.2mm, which is sufficient for most needle-based interventional therapy.

2.6 Conclusion

A modular design approach is utilized in this MRI compatible needle driver to control delivery of various tubular shaped surgical tools, including straight needle insertion, asymmetric tip needle steering or compensation, and concentric-tube placement. A cylindrical helix imaging coordinate registration fiducial frame is integrated into the needle

driver to visualize and localize the robot in MRI image space directly and in a real-time fashion, and thus potentially improve the workflow and enhance the accuracy of the surgery. Finally, the workspace verification and system accuracy evaluation were obtained by the needle driver experiment.

3. Development of Drive System For MRI-Guided Base Robot

3.1 Motivation and Goal

To date, needle based MRI compatible surgical robot has become a hot topic in cutting-edge research of percutaneous surgical interventions. There is no doubt that the choice of actuator, the core of the driving system, plays a significant role in MRI-guided surgical medical robot. There are several common nonmagnetic motors featuring for MRI compatible surgical robot interventions, such as PCB motor, PiezoMotor, NanoMotion motor and Shinsei motor.

The Shinsei motor is a kind of harmonic piezoelectric ultrasonic motor in Fig.3.1, which has the following characteristics:

a) Low speed and high torque. The maximum torque is 1 NM. As it allows high torque at low speed, direct drive is possible.

b) Nonmagnetic nature. Since the ultrasonic motor does not utilize magnetic power as its driving force, it does not generate magnetism. It further is available with a non-ferrous housing, which makes it MRI compatible.

c) High response and controllability. Small rotor inertia and braking performance due to motor friction realize incomparable responsiveness and controllability, making it have high precision.

d) Self-retention. As it is retentive even after the power is turned off, and electromagnetic brake is not necessary.

e) Compact, lightweight and quiet. As it has a simple structure, there is no coil and no magnet. Moreover, since its rotational speed is low to begin with, it is quiet even when gears are used, especially compared to the piezoelectric motor.

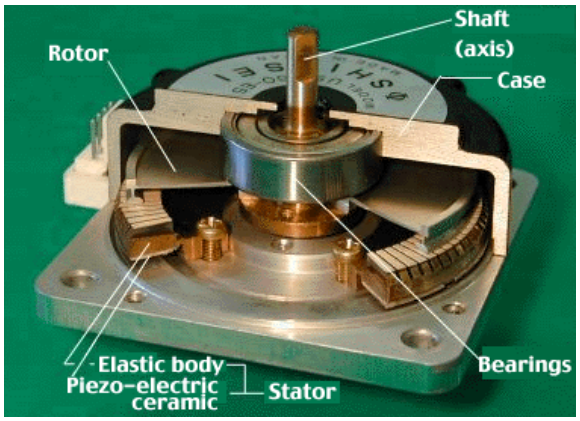

Figure 3. 1: USR60 Shinsei Motor [35]

With so many characteristics described, therefore, we chose the USR60 Shinsei motor (SHINSEI corporation, Japan) to drive base robot. The final goal is to drive the Shinsei motor successfully in order to achieve multiply degrees of freedom movement of the base robot.

3.2 Shinsei Motor

Ultrasonic motor is an available concept of driving device these years, transferring electric energy to ultrasonic vibration using the converse piezoelectric effect of piezoelectric materials and achieving axial rotation and linear translation through friction method. The structure is shown in Fig.3.2. The Shinsei motor consists of rotor and stator. The stator is made of elastic body and piezoelectric ceramic and rotor is made of metal plate. There is no coil and magnet inside this kind motor.

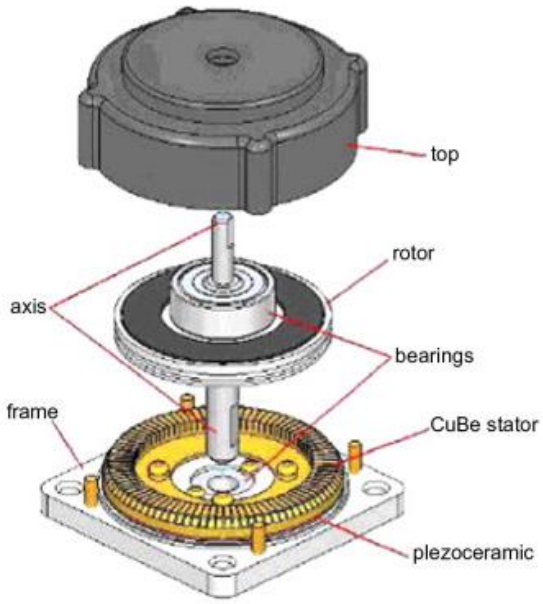

Figure 3. 2: Internal structure of Shinsei motor [36]

The motor principle is shown in Fig.3.3. When we provide two pieces of piezoelectric ceramic with two high frequency voltage, the elastic body will produce two standing waves. Then the two standing waves combine to one traveling wave, which is along circle direction of stator. It will produce ultrasonic vibration in stator. The proton of stator surface will form a certain trajectory, like elliptic trajectory. This kind movement drives rotor to move continuously via the friction between the stator and rotor. Commonly, this movement is micron order of magnitude.

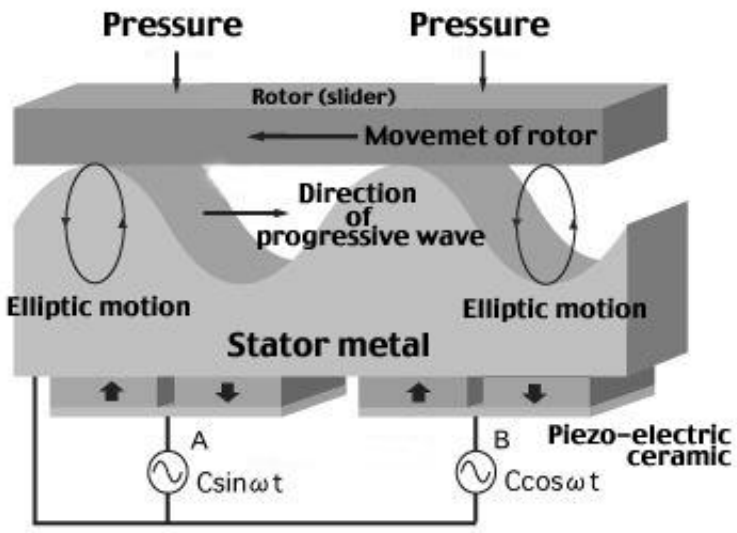

Figure 3. 3: Working principle of ultrasonic Shinsei motor [37]

When high frequency and high voltage signals are placed on piezoelectric ceramic, it can produce alternating telescopic deformation. The elastic body will produce standing waves shown in Fig.3.4. The equations of the two standing waves are shown in 3.1 and 3.2 [38]. The two standing waves can be described in Fig.3.5 [38].

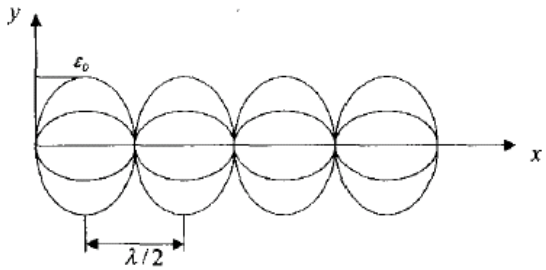

Figure 3. 4: Standing wave produced in elastic body [38]

(3.1) $$y_A = \varepsilon_0 \sin\frac{2\pi}{\lambda} x \sin\omega_0 t$$

(3.2) $$y_B = \varepsilon_0 \cos\frac{2\pi}{\lambda} x \cos\omega_0 t$$

In elastic body, the two standing waves combine into one travelling wave in equation 3.3 [38].

$$y = y_A + y_B = \varepsilon_0 \cos\left(\frac{2\pi}{\lambda}x - \omega_0 t\right) \tag{3.3}$$

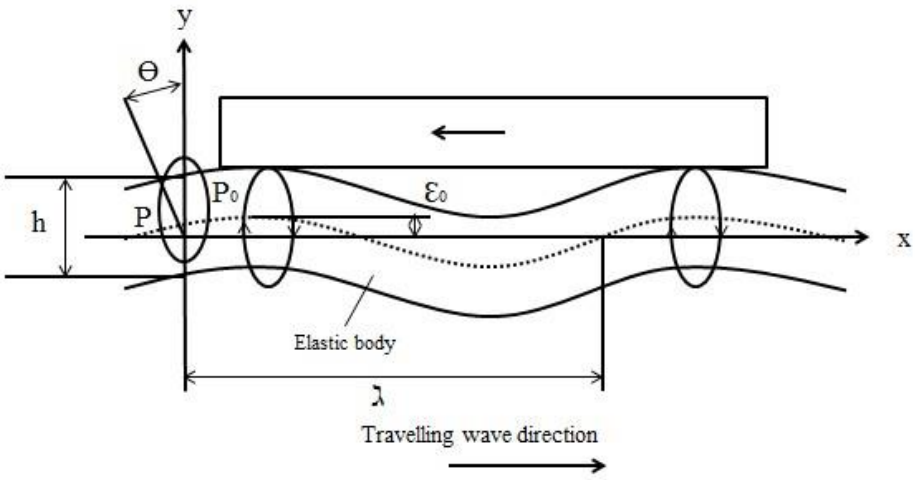

Figure 3. 5: Travelling wave along the stator [38]

Let's assume thickness of elastic body is h. The distance from P0 to P in x direction is shown in equation 3.4 [38]. The result of Θ is shown in equation 3.5 [38]. The distance from P0 to P in x direction is shown in equation 3.6 [38].

$$\varepsilon_x \approx -\frac{h}{2}\sin\theta \approx -\frac{h}{2}\theta \tag{3.4}$$

$$\theta = \frac{dy}{dx} = \varepsilon_0 \frac{2\pi}{\lambda}\cos\left(\frac{2\pi}{\lambda}x - \omega_0 t\right) \tag{3.5}$$

$$\varepsilon_x = -\pi\varepsilon_0 \frac{h}{\lambda}\cos\left(\frac{2\pi}{\lambda}x - \omega_0 t\right) \tag{3.6}$$

The lateral movement velocity of surface particle in elastic body is in equation 3.7 [38].

(3.7) $$v_p = \frac{d\varepsilon_x}{dt} = -\pi\omega_0\varepsilon_0 \frac{h}{\lambda}\sin\left(\frac{2\pi}{\lambda}x - \omega_0 t\right)$$

Therefore, the velocity of motor has a relationship with the frequency of sin voltage wave. We can achieve velocity adjustment by changing frequency of sin wave.

3.3 System Requirement

3.3.1 Piezoelectric Board

In Automation and Interventional Medicine Lab, the piezoelectric motor driver board has been previously developed and implemented to drive the piezoelectric motors [39&19] as shown in Fig.3.6. The stator of PiezoLegs motor consists of four quasi-static legs (A, B, C and D leg), which are friction based. When four channels of sin waves are placed on four ceramic legs of the piezoelectric motor, all legs are electrically activated and they are elongated and bending. The motion of motor is transferred through contact friction between the drive leg and the drive disc.

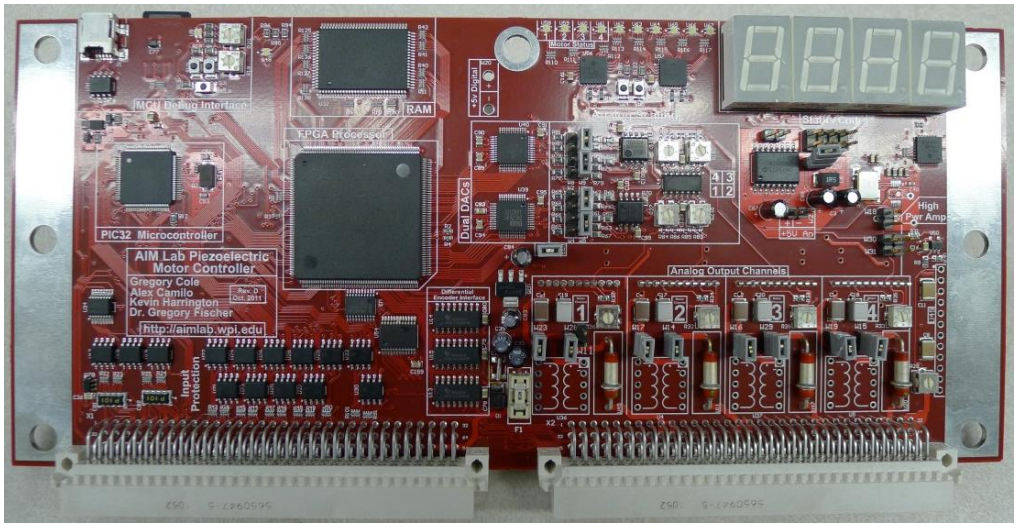

Figure 3. 6: Surface of Piezoboard developed previously in the AIM Lab

The four channels of driving sin waves are generated through the piezoboard and its schematic diagram is shown in Fig.3.7.

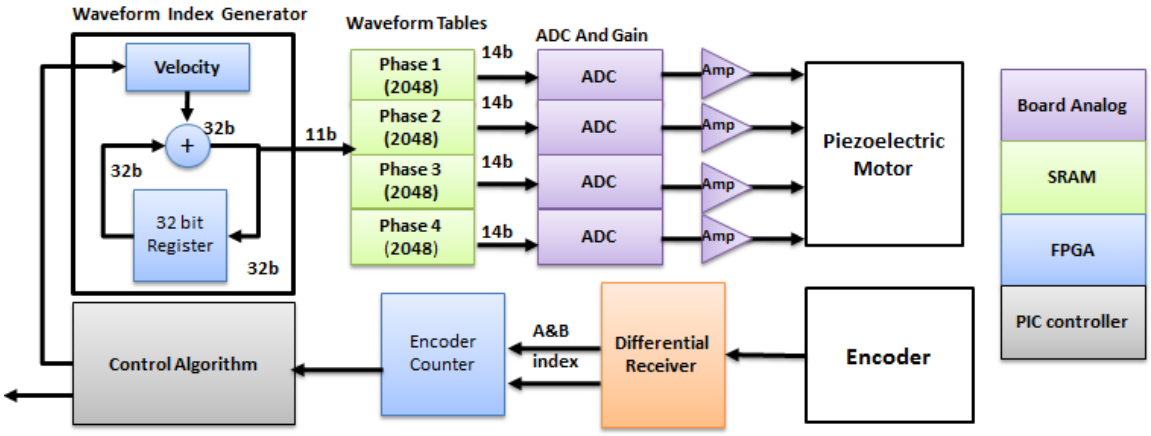

Figure 3. 7: General function diagram of piezoboard [39&19]

A four-channel high power arbitrary waveform generator was developed and implemented to run piezoelectric actuators. The working flow is summarized in the following steps:

a) The field-programmable gate array (FPGA) has a 32-bit add register. The register will add n each time when the clock signal comes. Finally, we can obtain a linear relationship line shown in Fig.3.8.

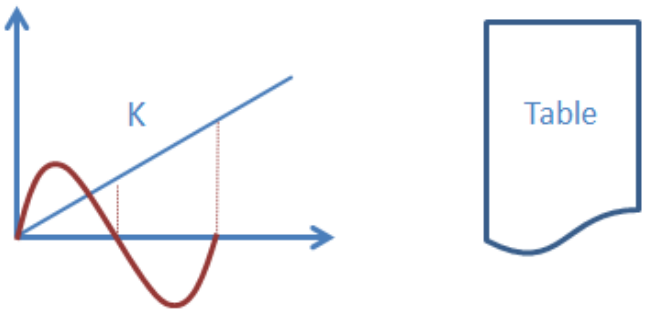

Figure 3. 8: Linear line for FPGA and look up table

b) The SD card stores a sin table inside. The PIC microcontroller will load sin waveform from SD card based on the linear line produced in the FPGA. We can change the wave frequency via modifying the value of n.

c) The four channels analog waveform is then streamed in analog to digital converter to obtain the digital waveform signals. Then the wave signals will be amplified through three stage amplifiers. The final four channel waveforms drive the piezoelectric motors.

d) The optical encoder detects the moving of the motor and the differential signal is sent to PIC microcontroller. The PIC microcontroller receives an input in the form of position or velocity and then set a certain point for the FPGA generator, achieving control loop.

3.3.2 Requirement

The maximum output voltage of the pizeoboard is 48 V, and was originally design specifically for the low voltage Piezo Legs motors. The major requirement for the high power Shinsei motors is that sine wave signal voltage should be increased to 350 V (peak to peak) to drive the ultrasonic motor. In addition, the new PCB board should be implemented into the backplane board (shown in Fig.3.12) to corporate with the pizeoboard. The backplane board provides with 96 pins connectors for pizeoboard plugging in. The new PCB would be placed parallel to the pizeoboard, therefore, the electric signal should be stable and unaffected by other boards. The requirements are listed as follows:

1) Increasing the waveform voltage from 24V to 350V
2) Filtering the AC signal from the sine waveform
3) Minimizing influence of input and output signal to peripheral system
4) Physically fitting in the backplane board

3.4 Circuit Design and Test

3.4.1 Solution

Both piezolegs motor and Shinsei motor share the similar mechanism, driving the stators with different phase of high frequency sin wave voltages. Both of them achieve motion by the friction between stators and rotors. In piezoelectric board, a kind of four channels of sin waveforms synthesizer has been demonstrated and implemented for the piezoelectric motor. Therefore, the drive system for Shinsei motor can be achieved by imitating its high frequency sin waveforms generator. The adjacent two sin waveforms will be chosen from the piezoelectric board and a waveform adjustment circuit will be developed and implemented to obtain two phases of waveforms required for Shinsei motor as shown in Fig.3.9.

The output waveform voltage of pizeoboard ranges from 0 to 48v and maximum output power is 480 w. The specification of Shinsei motor shows that the driving voltage is 350 v and the working current is less than 1A. Therefore, the available approach is to use the transformer to increase the waveform voltage.

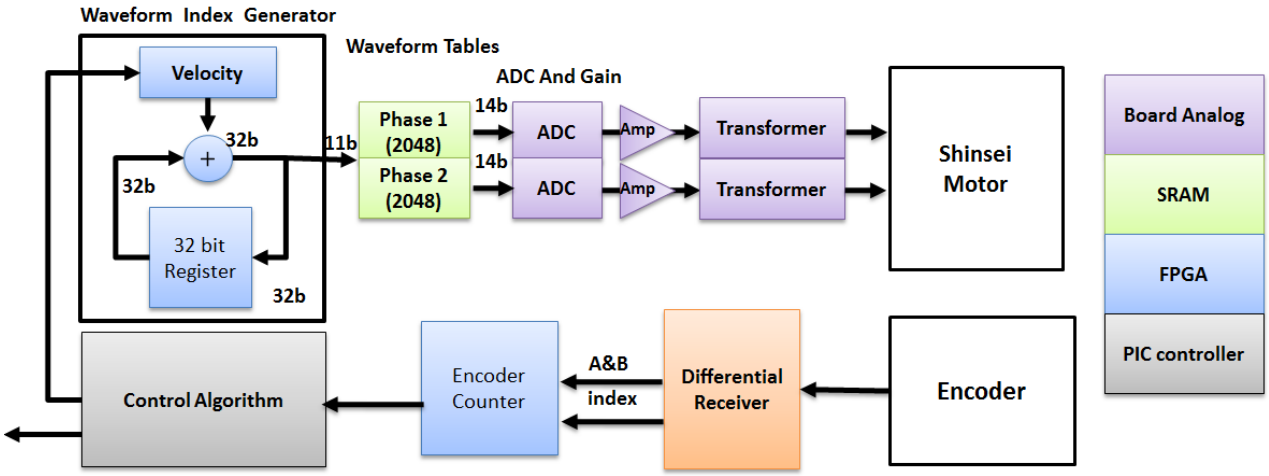

Figure 3. 9: General function diagram of driving system for ultrasonic shinsei motor

3.4.2 Design and Test

A transformer is a static device that transfers energy from one circuit to another without any direct electrical connection and with the help of mutual induction between two windings. A varying current in the primary winding creates a varying magnetic flux in the transformer's core and thus a varying magnetic flux through the secondary winding. Then this varying magnetic flux induces a varying voltage in the secondary winding. Fig.3.10 shows the structure of basic transformer. The instantaneous voltage follows $\frac{Vp}{Vs}=\frac{Np}{Ns}$. N_p is the number of turns in the primary coil and N_s is the number of turns in the secondary coil.

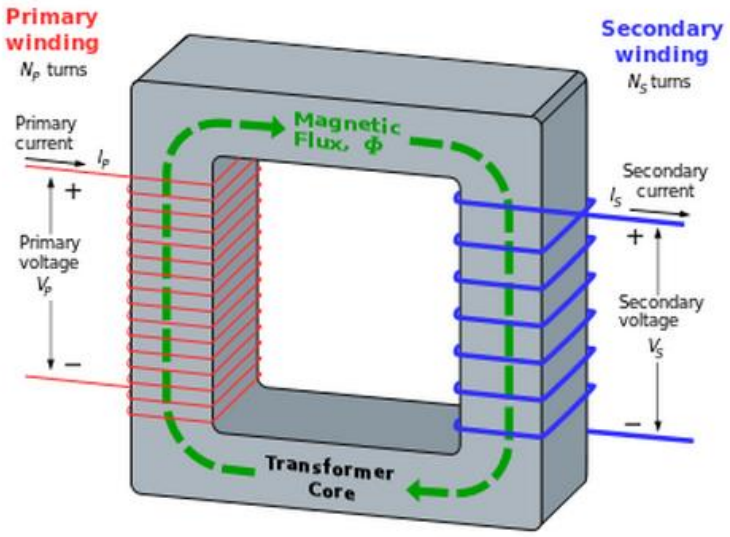

Figure 3. 10: Schematic for the basic transformer [40]

The transformer used in this design has two coil ratios 1:7 and 1:14. The circuit is shown in Fig.3.11. A capacitor was integrated before the primary coil to filter the AC signal. The capacitor can endure maximum current 2A.

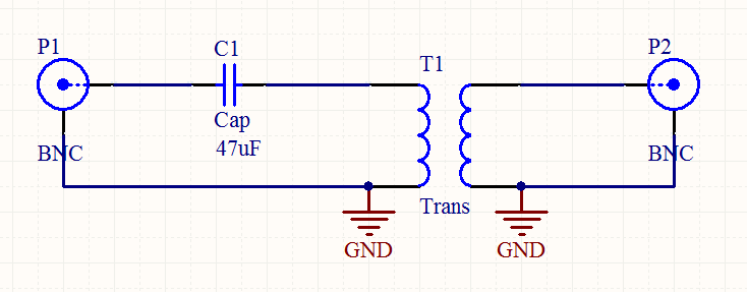

Figure 3. 11: Circuit schematic of transformer board

A lab environment test has been performed using pizeoboard, backplane board, transformers and Shinsei motor shown in Fig.3.12. The system can drive motor move forward and backward.

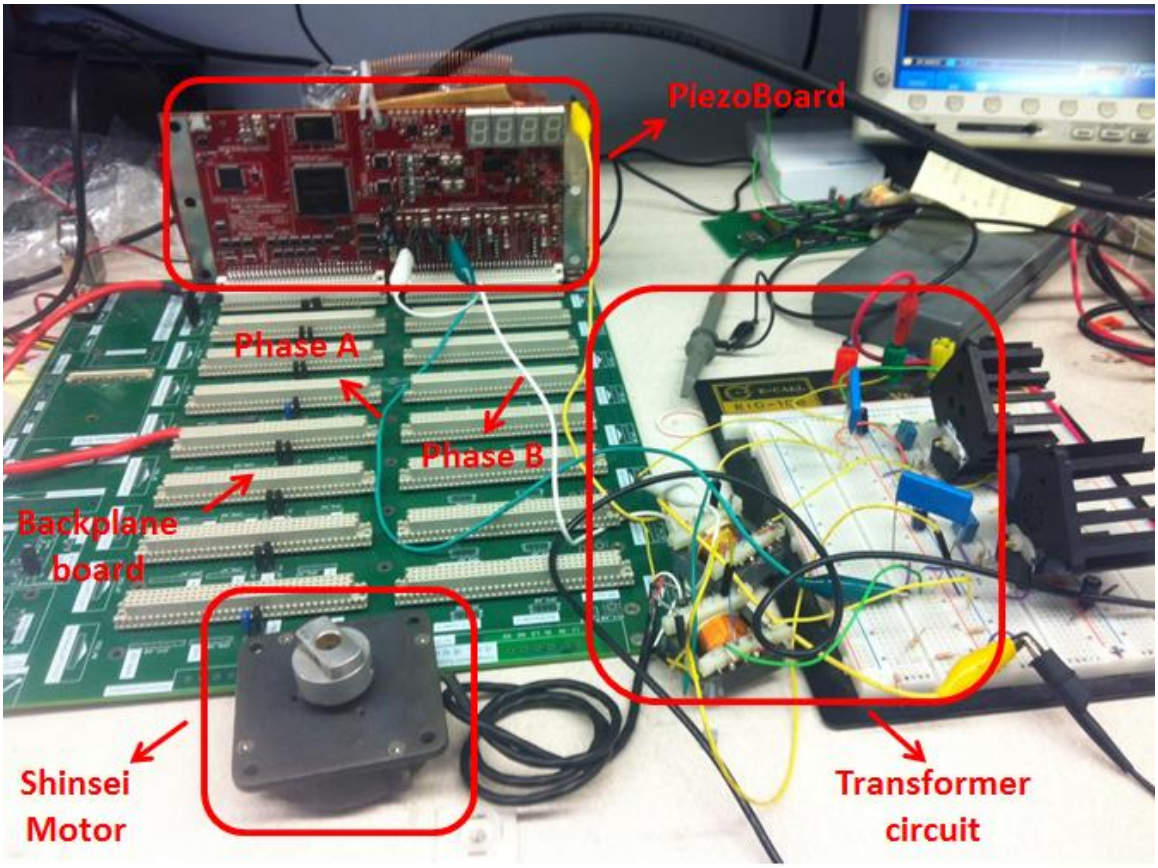

Figure 3. 12: Test driving system in breadboard

3.4.3 Transformer PCB Board and Test

3.4.3.1 PCB Board Design

The purpose is to design a transformer PCB and integrate the function board into the backplane board parallel to piezoelectric board. Then all the controller boards will be placed into the MRI-compatible controller box showed in Fig.4.2. The general schematic diagram is shown in Fig.3.13. The base robot has 4 independent movement legs, with each one driven by one Shinsei ultrasonic motor. For each Shinsei motor, two channels of high frequency voltage waveforms are required to generate ultrasonic vibration along the stator. Eventually, the transformer board consists of four channels motor driving signals and each channel is integrated with two phase waveforms.

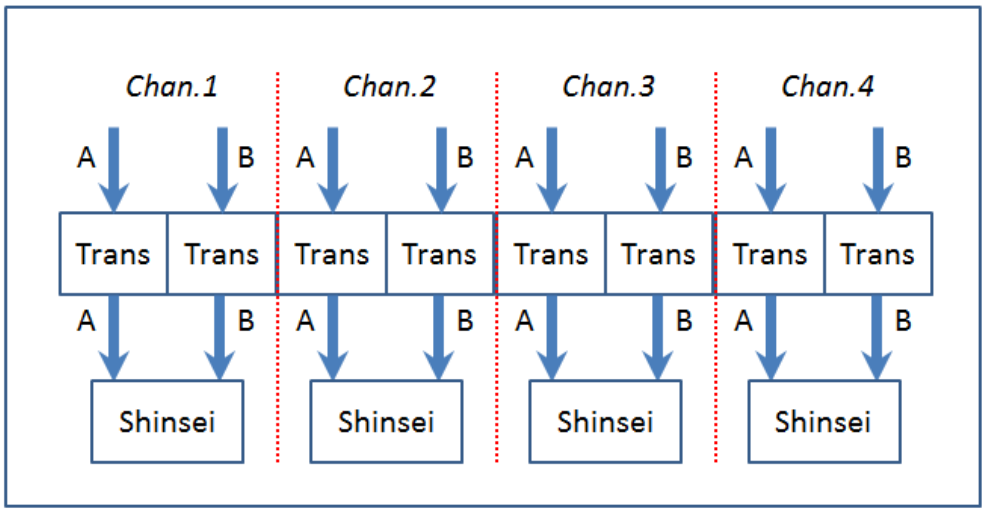

Figure 3. 13: General function schematic of transformer board

The waveform signals streamed out from piezoelectric board will be transmitted using coaxial cable in order to reduce the high frequency interference to imaging. As shown in Fig.3.14, the coaxial cable consists of four layers: center core, dielectric insulator, metallic

shield and plastic jacket. The center core is designed for real transmitted signal and it is separated with metallic shield by dielectric insulator. The cable is protected by an outer insulating jacket. Normally, the shield is kept at ground potential and inner center core is used to transmit the electric signal. One good reason of this coaxial design is that the magnetic and electric fields are confined to the dielectric insulator with little leakage outside the shield. Meanwhile, magnetic and electric fields outside the cable are largely kept from causing interference to signal inside the cable. The choice of this coaxial cable will increase the stability of this transformer board.

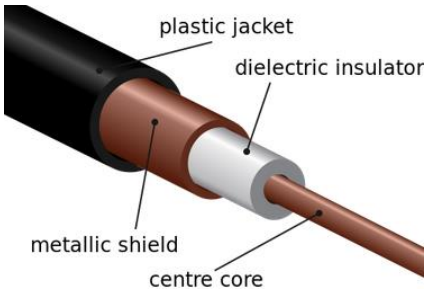

Figure 3. 14: Structure of coaxial cable

At the end of coaxial cable, the coaxial connector is used and implemented in transformer board. From the Fig.3.15, the central pin is for signal with four shielded ground pins surrounded.

Figure 3. 15: Coaxial connector

As mentioned in previous description, the transformer board will be placed on the surface of backplane board, parallel to piezoelectric board. According to the piezoelectric board, it is connected and fixed in backplane via 96-pin connector shown in Fig.3.16. The transformer board is fixed on backplane board using 96-pin connector. In order to ensure the stable of transformer board, grounded pins are connected to GND same as the piezoelectric board and the rest pins are left unconnected.

Figure 3. 16: 96-pin connector

The final transformer PCB board is shown in Fig.3.17.

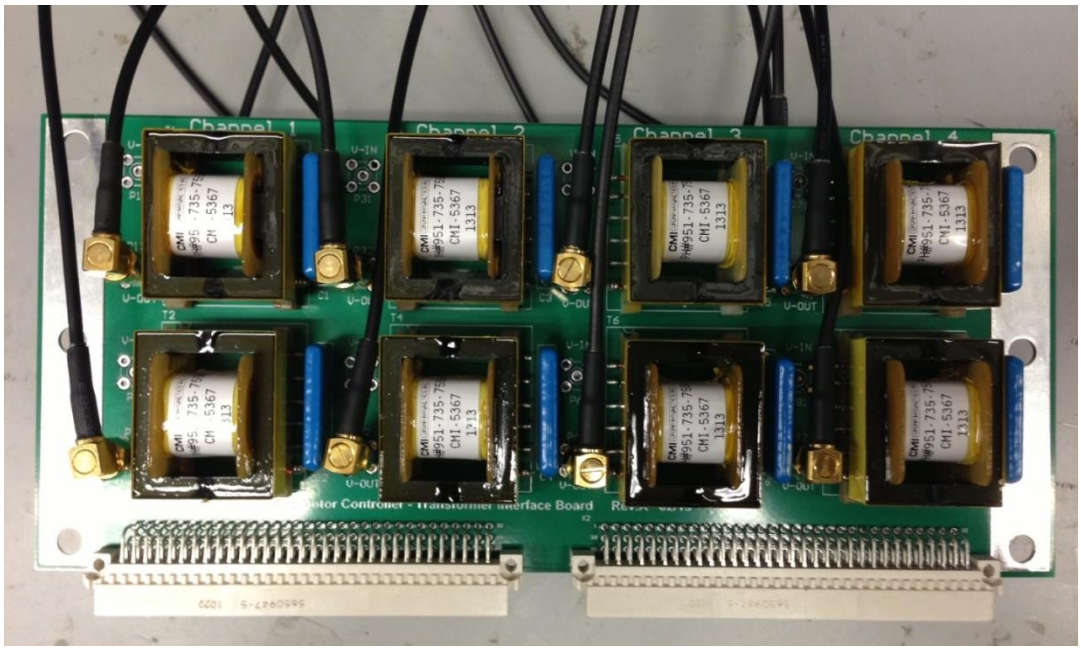

Figure 3. 17: Transformer PCB board

3.4.3.2 Board Test

This experiment was performed to evaluate the function of Shinsei motor drivering system. The test system contains control software, backplane board, pizeoboard, transformer board and Shinsei motor and interface board shown in Fig.3.18.

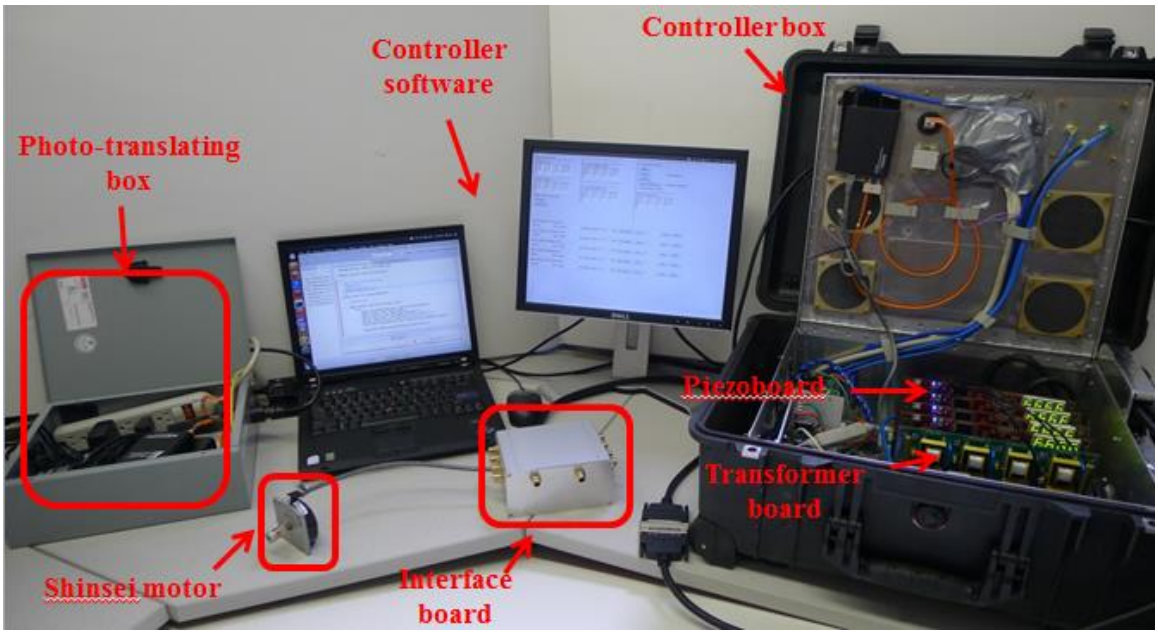

Figure 3. 18: Final driving system test for ultrasonic Shinsei motor

The software and hardware system can directly drive the motor forward. The waveforms of the channel signals were displayed in Fig.3.19. These two sine waves are 392V with 90 degree phase difference and 39.8 kHz frequency. The motor can also been driven to move backward with the two sine waves swapping. The velocity of Shinsei motor can also be adjusted through changing the frequency of sine waveform.

Figure 3. 19: The two waveforms for ultrasonic Shinsei motor

3.5 Conclusion

A hardware controller system was introduced and improved for control of ultrasonic Shinsei motor which is integrated in base robot under the modular needle driver. According to the schematic of the Shinsei motor, two high frequency voltage waveforms were generated using the piezoelectric board. A new transformer board was designed to cooperate with piezoelectric board to achieve motion of base robot legs. The whole system was integrated and tested, and can drive the ultrasonic Shinsei motor forward and backward. In addition, Shinsei motor's speed can also be adjusted through changing the frequency of the high frequency voltage.

4. Development of Robot Interface Board For MRI-Guided Controller System

4.1Motivation and Goal

A schematic of the base robot upon which the needle driver will be mounted is shown in Fig.4.1, which is designed by Johns Hopkins University. There are four robot legs sliding on two parallel rails. These four legs can move separately so that the base robot can achieve different height and different slant angle. On top of the central platform stands the MRI compatible needle driver for percutaneous interventions. The weight of base robot and needle driver is too heavy, which makes the system unsafe and unstable if any of the four legs moves out of its range, especially during the surgical operation. In addition, the Shinsei motors are very powerful and may break something if they get to the end of its range. Therefore, the limit security system is vitally significant and necessary for this base robot system to ensure its stability and safety.

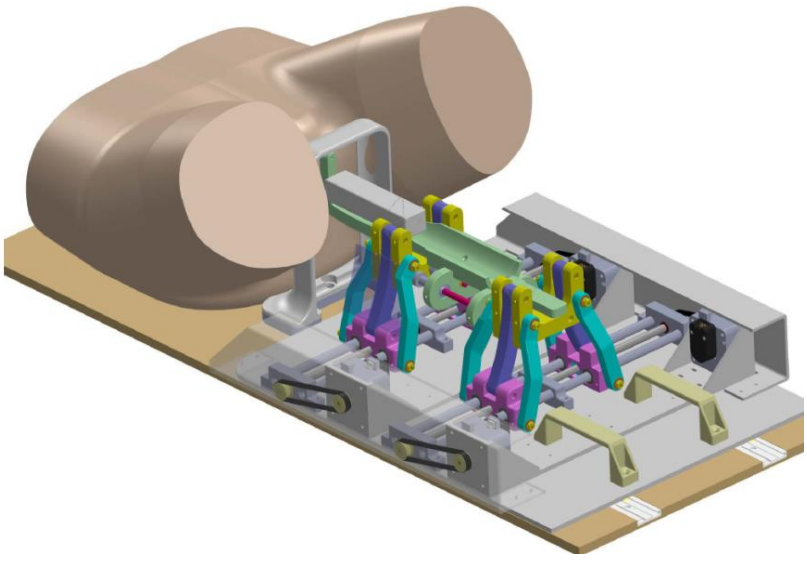

Figure 4. 1: Structure diagram of base robot [Johns Hopkins University]

Limit switch is a switch operated by the motion of a machine part or presence of an object, which can be used for control of a machine as safety interlocks. The initial solution is to assemble two fiber optic limit switches for each base robot leg, with each one placed at two sides of the robot leg. Finally, as long as any one leg works out of its range, the optical limit switch will generate a stop control signal to central control system, which will force to stop the motor movement.

4.2 System Requirement

According to the goal described above, this interface board should be integrated with four channels of limited switches for the four base robot legs and each channel should contain two limit switches. Therefore, there are totally eight optical limit switches. Four legs means that four couples of motors and encoders connectors should be included on the board and another four external encoders connectors should also be integrated.

The motor controller system is assembled in control box in Fig.4.2. The controller box connects to the motors and encoders integrated in the medical robot through a 68-conductor shielded twisted pair VHDCI cable. Therefore, the interface board will be placed between the controller box and medical robot via VHDCI connector. If the VHDCI connector of controller box connects interface board, all the motors, encoders should be connected to this interface board, indirectly connecting to controller box. In this situation, the eight channel limit switch should take the same connector with external encoder, which bringing in security problem for these two functions. Both optical limit switch and external encoder will use

differential driver working at different time. Therefore, the design circuit should protect one when the other is working.

As this system will be placed in MR space, the electronic signal of interface board would end up with MRI image distortion. Meanwhile, the strong magnetic field would also interfere with electronic signal in the interface board. Consequently, an aluminum enclosure is required to keep the interface board shielded from outside magnetic field.

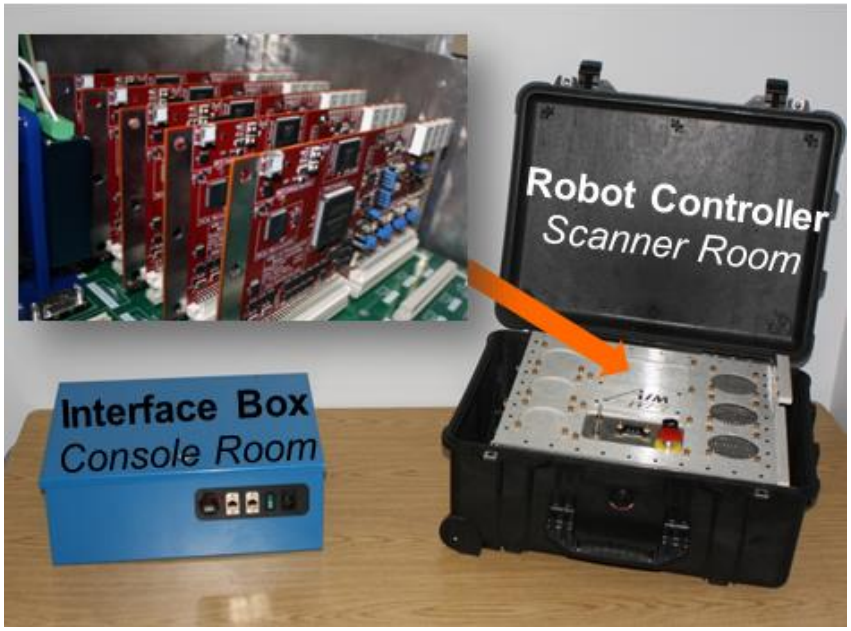

Figure 4. 2: Medical robot control box previously developed [48]

The primary requirements for this interface board are:

1) Integrating eight channels of optical limit switch circuits for four base robot legs
2) Offering four connector channels of motors and encoders for four base robot legs
3) Offering another four connector channels for external encoders
4) Making sure the safety between limit switch differential driver and external encoder differential driver
5) Placing the robot interface board with an aluminum enclosure for RF shielding

4.3 Circuit Design and Test

Optical limit switch, also known as optical sensor, is operated to detect the presence of an object via detecting the reflected or blocked light from the objects shown in Fig.2.18. It commonly consists of three parts including transmitter, receiver and detection circuit. In this design, the LED is chosen to emit light and the photodiode is utilized to detect light, which convert the physical signal to electric signal. The movement of the leg would interfere with light path of LED, which affects the detected light for photodiode. The photodiode signal goes through the detection circuit system and eventually produces a jumping signal for the central control system.

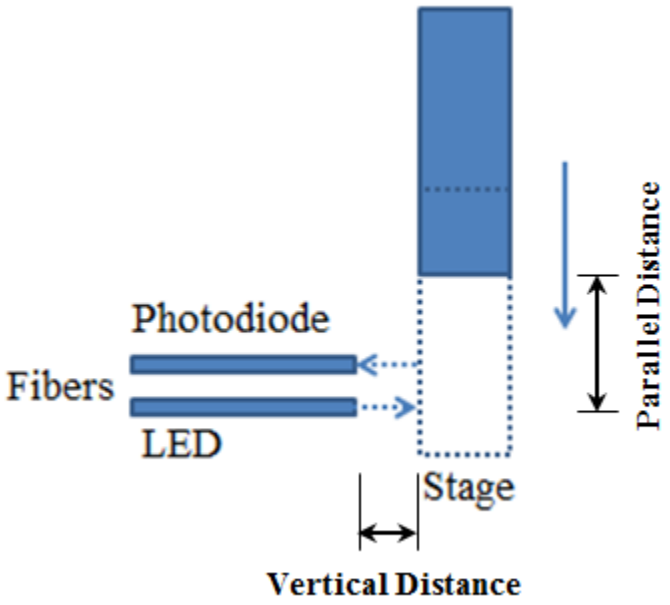

Figure 4. 3: Schematic of optic limit switch

4.3.1 LEDs and Photodiode

In Fig.4.4, blue component is IF-E91A (Industrial Fiber Optics, Tempe, AZ), an infrared LED in a “connector-less” style plastic fiber optical package. This LED is a high-output

medium-speed infrared LED, whose output spectrum peaks at 950 nm. There is a micro-lens inside the optical package, and a precision molded PBT housing ensures efficient optical coupling with standard 1000 um plastic fiber cable. From the datasheet, the typical forward voltage is 1.2 V with the current of 20 mA. The typical forward voltage is 1.27 V with the current 50 mA. In addition, the max forward voltage is 1.6 V [41]. The black component is IF-D91 (Industrial Fiber Optics, Tempe, AZ), a high-speed photodiode detector housed in a "connector-less" style plastic fiber optic package with its optical response ranging from 400 nm to 1000 nm, typically in 960 nm. The detector package features an internal micro-lens and also a precision-molded PBT housing to ensure efficient optical coupling with standard 1000 um core plastic fiber cable [42].

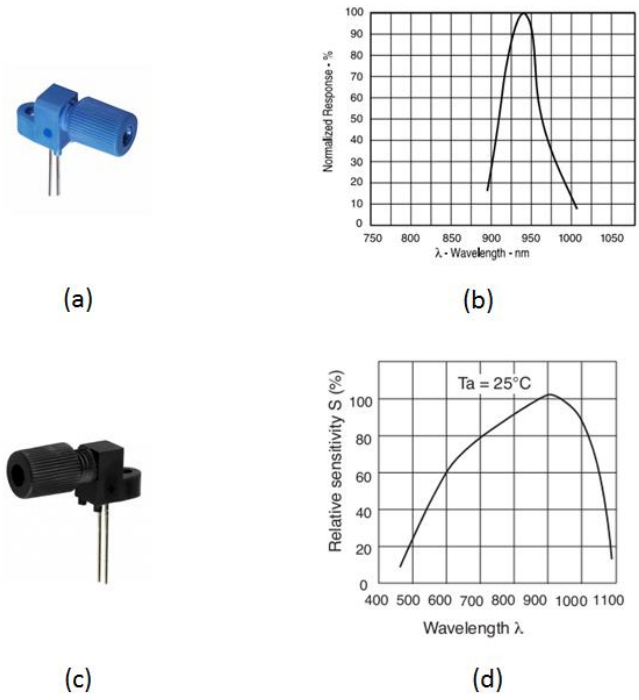

Figure 4. 4: (a) IF-E91A LED (b) Typical LED spectral output vs. wavelength [41] (c) IF-D91 photodiode (d) Typical photodiode detector response vs. wavelength [42]

From Fig.4.5, our living space ranges from cosmic and gamma rays to radio waves, with its frequency decreasing gradually. It is shown that visible light features from 400 nm to 700 nm, which is main influential factor in outside environment. Therefore, avoiding the influence of natural visible light plays a significant role in optical limit switch circuit. However, the LEDs and photodiode peaks in infrared period, reducing possible influential factors to optical sensor and guaranteeing stability of optical system.

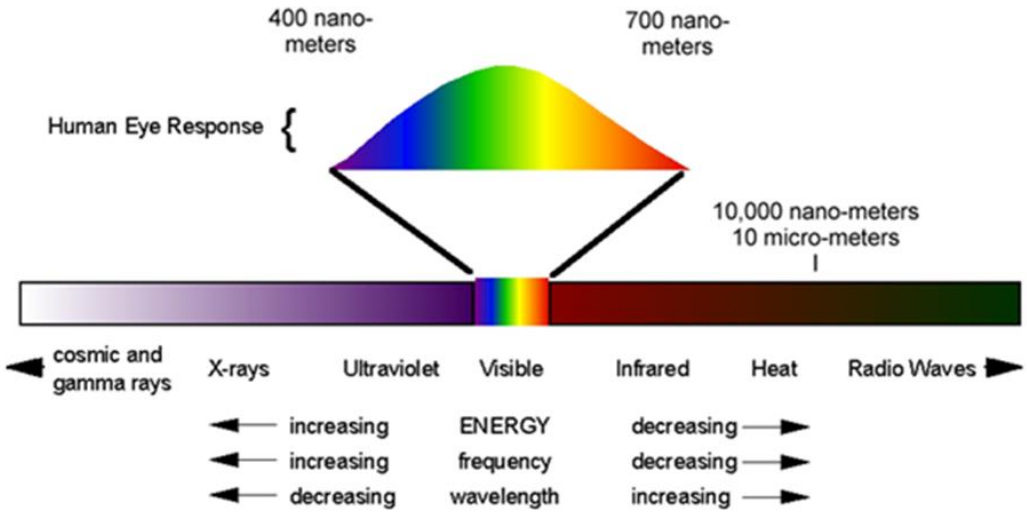

Figure 4. 5: Spectral distribution [43]

Before the limit switch circuit design, a simple test of the LED and photodiode was performed using a Cartesian stage in AIM lab, which has three degrees of freedom: X, Y and Z. One channel LED and photodiode was placed, followed by the simple amplifier shown in Fig.4.6. The LED fiber and photodiode was placed parallel, implementing with reflective method. The end of Cartesian stage was covered by smooth white label. When the fibers were covered by the white label stage, the photodiode fiber would detect reflective light from LED fiber.

Figure 4. 6: LED and photodiode test

The parallel distance (shown in Fig.4.3) between fibers and white label stage was ranged from -3.99 to 1.99 mm and used the digital multimeter to measure the output pin of amplifier. Each time the distance added 0.2 mm and read the voltage change from the digital multimeter. All the collected results are displayed in Table.3. Fig.4.7 is scatter diagram of this voltage table.

Table 3: The relationship between distance and voltage

No.	distance(mm)	voltage(v)	No.	distance(mm)	voltage(v)
1	-3.99	0.058	17	-0.79	0.714
2	-3.8	0.057	18	-0.61	0.825
3	-3.61	0.055	19	-0.41	0.921
4	-3.41	0.067	20	-0.21	0.989
5	-3.2	0.069	21	0	1.032
6	-3	0.072	22	0.2	1.057
7	-2.8	0.077	23	0.39	1.072
8	-2.59	0.082	24	0.6	1.078
9	-2.41	0.089	25	0.8	1.086
10	-2.19	0.104	26	1	1.09
11	-2.01	0.124	27	1.21	1.093

12	-1.81	0.161	28	1.39	1.093
13	-1.6	0.224	29	1.59	1.095
14	-1.4	0.314	30	1.81	1.097
15	-1.2	0.437	31	1.99	1.098
16	-0.99	0.574			

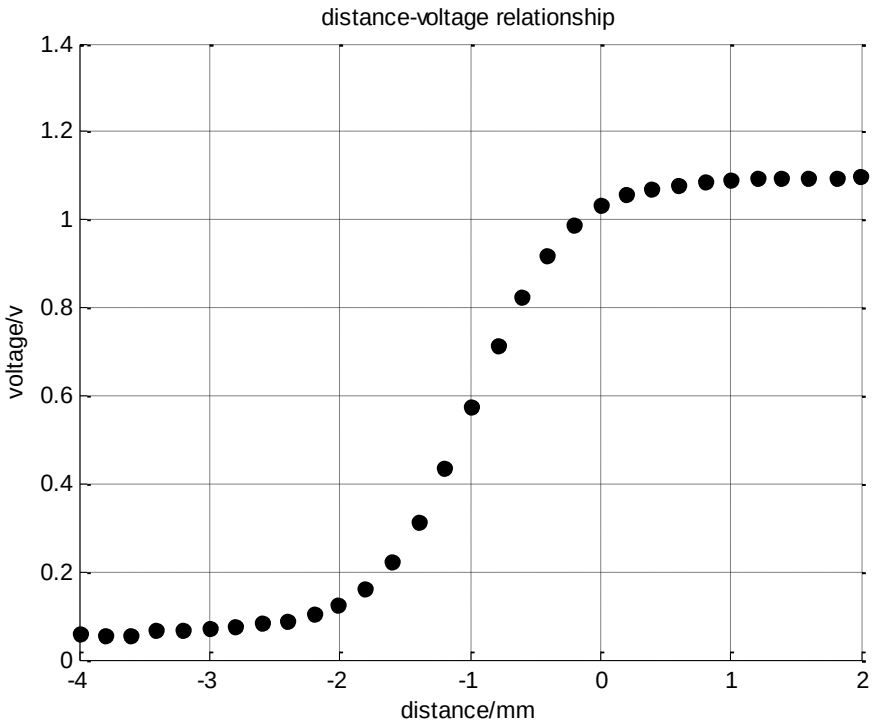

Figure 4. 7: Scatter diagram between voltage and distance

From the scatterplot, there is a significant change when the distance ranges, with the trigger point 1.032V at distance 0 (the stage just covers the led fiber port). In addition, a trigger point repeatability test was performed. The result displayed in Table.1. It shows that the LED and photodiode we chose has a perfect reliability.

Table 4: Trigger point repeatability test data

No.	distance(r	voltage(v)
1	-3.99	0.058
2	-3.8	0.057
3	-3.61	0.055
4	-3.41	0.067
5	-3.2	0.069
6	-3	0.072
7	-2.8	0.077
8	-2.59	0.082
9	-2.41	0.089
10	-2.19	0.104
11	-2.01	0.124
12	-1.81	0.161
13	-1.6	0.224
14	-1.4	0.314
15	-1.2	0.437
16	-0.99	0.574
17	-0.79	0.714
18	-0.61	0.825
19	-0.41	0.921
20	-0.21	0.989
21	0	1.032
22	0.2	1.057
23	0.39	1.072
24	0.6	1.078
25	0.8	1.086
26	1	1.09
27	1.21	1.093
28	1.39	1.093
29	1.59	1.095
30	1.81	1.097
31	1.99	1.098

	distance(mm)
1.01 v	0
	0.01
	-0.01
	-0.05
	-0.01
	-0.1
	-0.12
	-0.09
	-0.07
	-0.05
	-0.02
	-0.01
	-0.01

4.3.2 Limit Switch Circuit

The optical limit switch consists of transmitter, receiver and detection circuit. The general schematic diagram is shown in Fig.4.8. The photodiode detects signal from LEDs and the signal is sent to first amplifier, low-pass filter and second amplifier. Then the amplified signal goes through differential driver to produce stable signal for controller system.

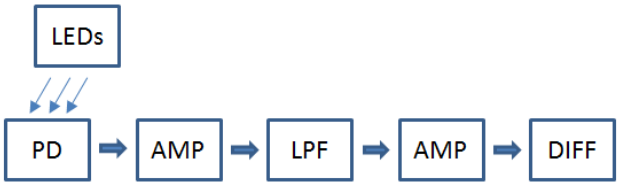

Figure 4. 8: Circuit schematic diagram of optical limit switch circuit

1) Transmitter

There are eight channel LEDs parallel with eight divider resistance 220 ohms in Fig.4.9. This module converts electric signal to optical signal.

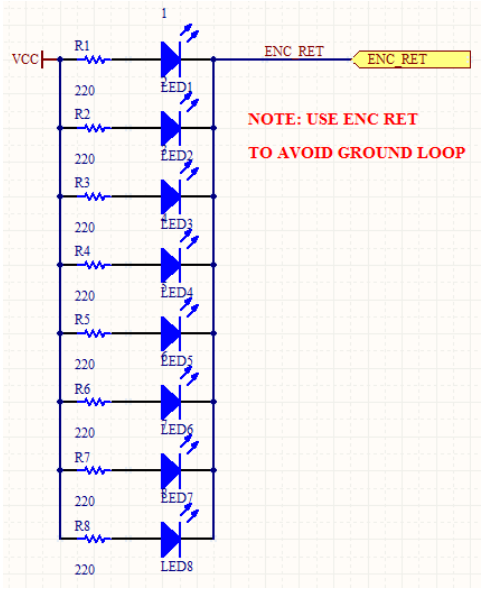

Figure 4. 9: Circuit diagram of eight channel LEDs

2) Receiver

The photodiode fiber receives the light reflected from the infrared LED. This detector converts optical signal to electric signal for the detection circuit.

3) Detection circuit

The amplifier used is AD8606 (Texas Instruments, TEXAS) made by Analog Device, which is single, dual and quad rail-to-rail input and output, single-supply amplifier. It features very low offset voltage, low input voltage and current noise, and wide signal bandwidth, making it

a perfect amplifier for photodiode application [44]. The chip and its pins are shown in Fig.4.10.

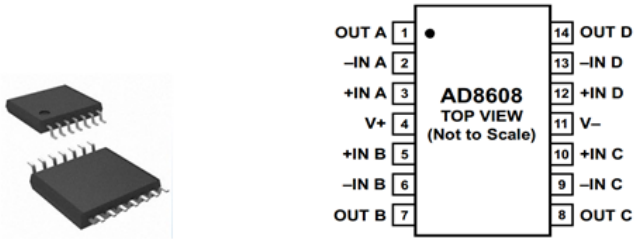

Figure 4. 10: Pins of AD8698 amplifier

The photodiode signal goes through the first stage amplifier and then goes through low-pass filter and finally goes through the second stage amplifier. Detailed circuit is shown in Fig.4.11.

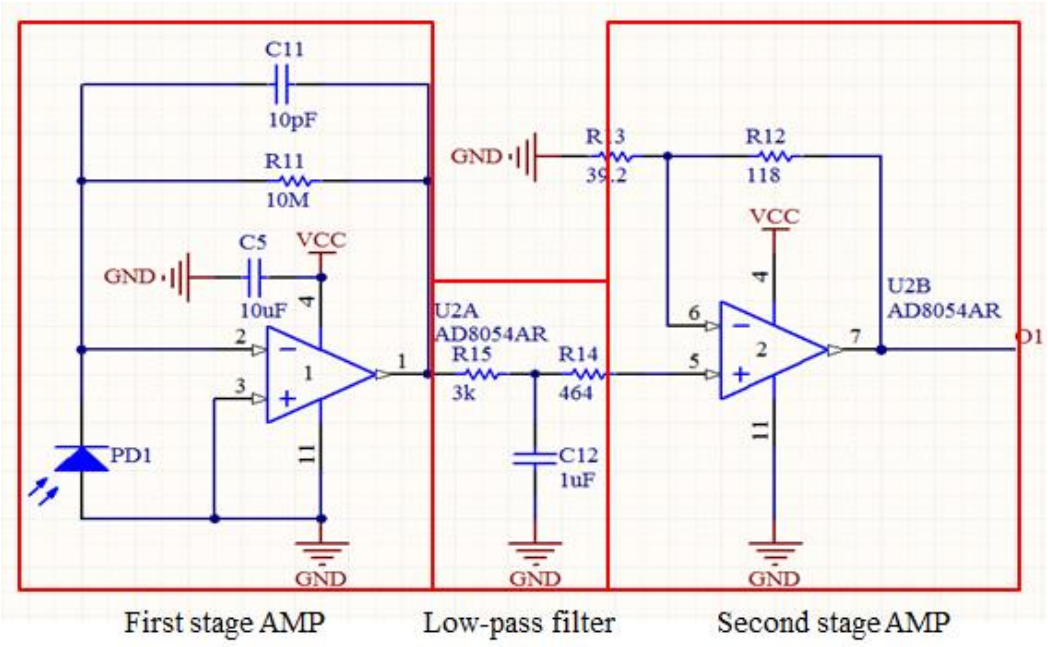

Figure 4. 11: Detailed circuit diagram of optical limit switch

The first stage amplifier, actual known as voltage follower circuit, is used to transfer a voltage from a first circuit, having a high output impedance level, to a second circuit with low input impedance level. This isolates the output circuit so the input is not affected in any way by the output device. Therefore, the voltage follower circuit works as a buffer without increasing the voltage at the same time. In addition, the capacity helps to filter the AC signal from the photodiode signal.

A low-pass filter is an electronic filter that passes low-frequency signals and attenuates signals with frequency higher than the cutoff frequency. The low-pass filter integrated in the detection circuit is passive electronic realization, which consists of a resistor in series with a load, and a capacitor in parallel with the load. When the higher frequencies go through, the reactance drops and the capacitor functions as a short circuit. However, when the lower frequencies go through, the capacitor exhibits high reactance and causes the lower frequencies to go through the load instead. In this simple low-pass filter, the cutoff frequency is given as $f_{cutoff}=\frac{1}{2\pi RC}$=53 Hz. Therefore, the majority of the high frequencies above the cutoff frequency, known as the noise signals, have been filtered to guarantee the circuit stability.

The second stage amplifier is a non-inverting amplifier with negative feedback, which combines a fraction of the output with the input so that a negative feedback opposes the original signal. In this configuration, the input voltage signal is applied directly to the non-inverting input terminal which means that the output gain of the amplifier becomes “positive” in value. The result of this is the output signal is “in-phase” with the input signal. The negative feedback configuration produces a non-inverting amplifier circuit with super good

stability, a high input impedance and a low output impedance. The final output of non-inverting amplifier is $u_o=\left(1+\frac{R13+R12}{R12}\right)u_i=4$.

The AM26C31I (Texas Instruments, TEXAS) in Fig.4.12 is four complementary-output differential line drives, which can offer the choice of an active-high or active-low enable input [45]. The function table is shown in Table 5.

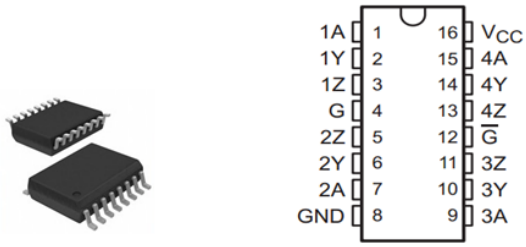

Figure 4. 12: Pins of AM26C31I differential driver

Table 5: Function table of differential driver

INPUT	ENABLES		OUTPUTS	
A	G	$\overline{G}$	Y	Z
H	H	X	H	L
L	H	X	L	H
H	X	L	H	L
L	X	L	L	H
X	L	H	Z	Z

Actually there is a voltage trigger input of the differential driver with the value 1.16 V. If the input signal is higher than 1.16V, the output signals are 1 and 0. If the input signal is lower

than 1.16V, the output signals are 0 and 1. The two output signals would guarantee the stability of optical limit switch signal as shown in Fig.4.13.

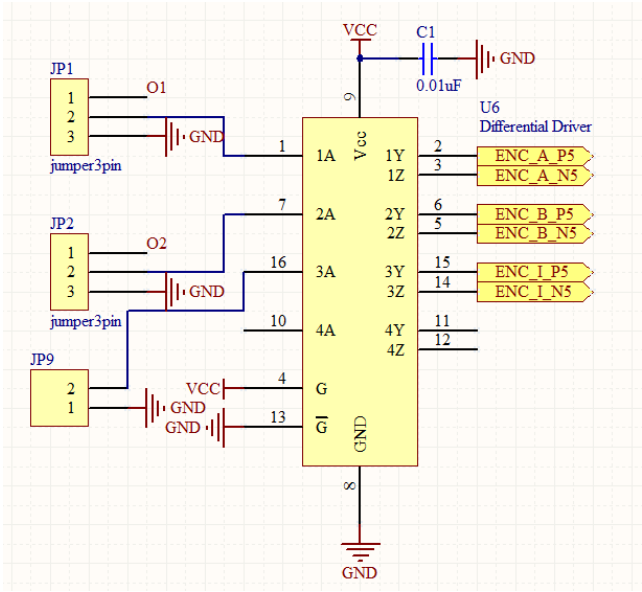

Figure 4. 13: Detailed circuit diagram of differential driver

One channel optical limit switch circuit was connected in the bread board shown in Fig.4.14. When the stage covers two parallel fiber ports, the final differential driver output signal will jump from 0 to 4.5 V, a perfect control signal for control system.

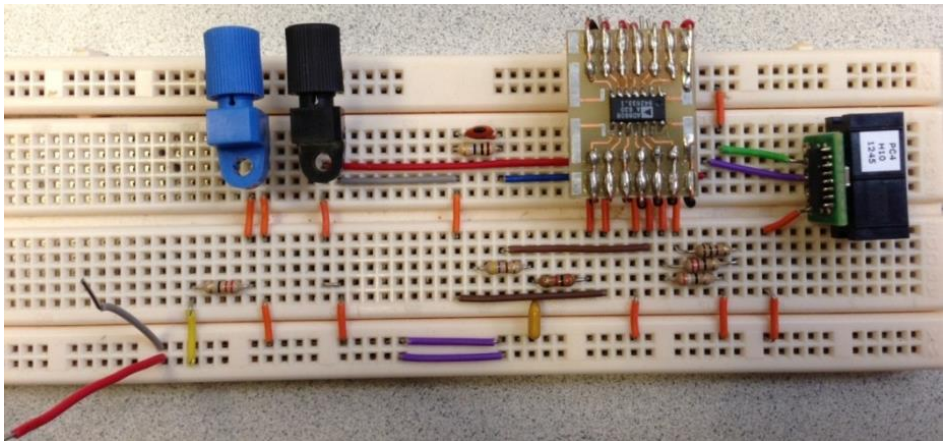

Figure 4. 14: Optical limit switch circuit in breadboard

4.4PCB Board Design and Test

4.4.1 PCB Board Design

After one channel testing in bread board, a PCB was designed using Altium Designer. The interface board integrated eight channels limit switches and transferred control signal to PiezoBoard via VHDCI connector. The interface board also offers four channel motor and encoder connectors and connects to PiezoBoard via VHDCI connector. In addition, this interface board achieves four external encoders plugging in, master signal for example. Fig.4.15 shows the general schematics for interface board.

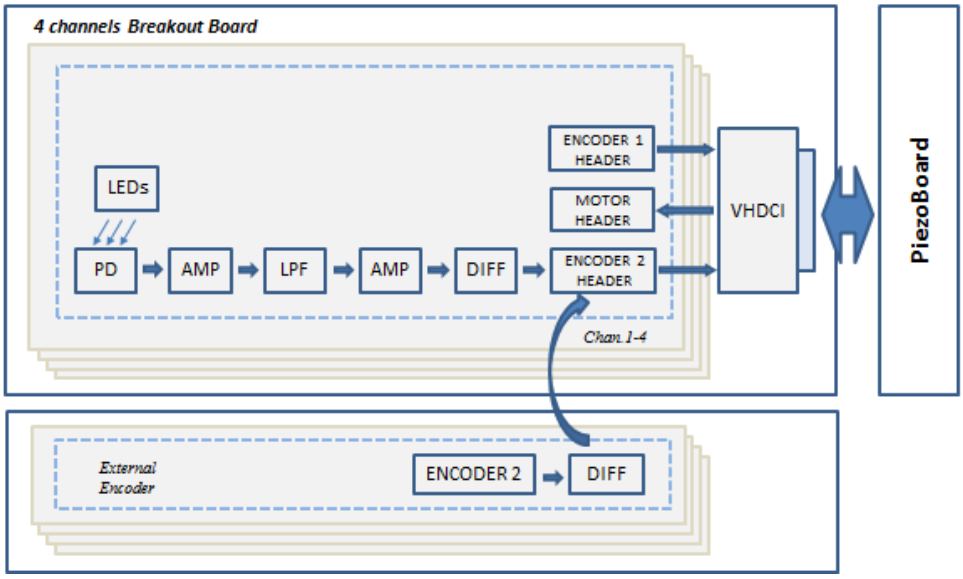

Figure 4. 15: The general schematic for four channels interface board

In this design, the eight channel limit switches shared the connectors with external encoder connectors. If external master's encoders signal is plugged in, this connection will risk in damaging the differential drivers in interface board, for the current probably backward to output pins of differential driver. From Fig.4.16, we can set the enable signal G and

$\overline{G}$ to get high resistance state in order to avoiding damaging the onboard chips. A four pins jump was designed in the PCB board shown in Fig.4.16. If the limit switch works, G connects to +5 V and $\overline{G}$ connects to GND. Otherwise, if the external encoder functions, G connects to GND and $\overline{G}$ connects to +5 V.

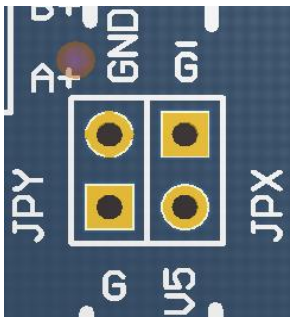

Figure 4. 16: Four pins jumper

The final interface board was populated and shown in Fig.4.16.

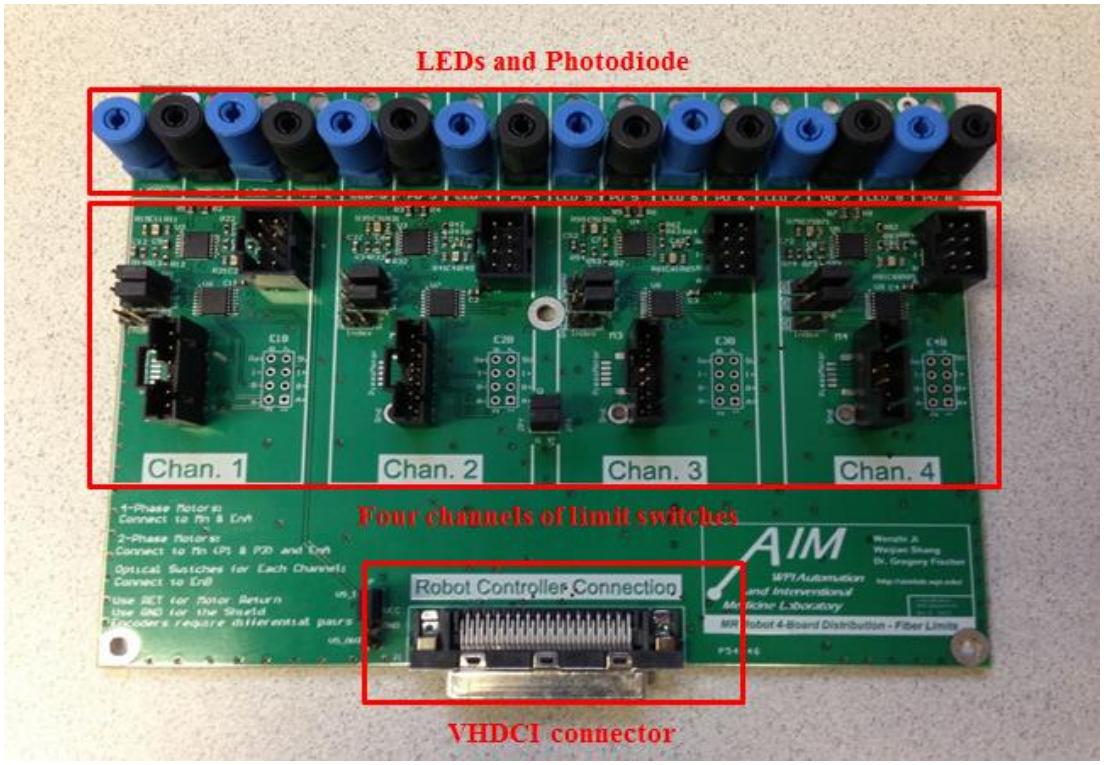

Figure 4. 17: Four channels interface PCB board

4.4.2 Aluminum Enclosure

An aluminum enclosure was ordered to cover the robot interface board, limiting electrical noise from escaping that the MRI scanner antennas pick up. During the operation, the enclosure should be sealed. All the motor, encoder and fiber cables should be wired outside through the mechanical holes. The through holes components in this enclosure are ¼ inch reducer and ¼ inch male connector shown in Fig.4.18. The reducer and connector can be connected tightly via the thread to fasten the aluminum plate.

Figure 4. 18: Reducer and connector

Four holes in each side were designed for four motor and encoder cables. Two holes in front side were designed for sixteen fiber cables. The total ten holes were machined using the drill machine. All the signal wires go through the holes with shield wires connected to the aluminum enclosure. In addition, another squared hole should be machined using milling machine for VHDCI connector. Therefore, the final aluminum enclosure was shown in Fig.4.19.

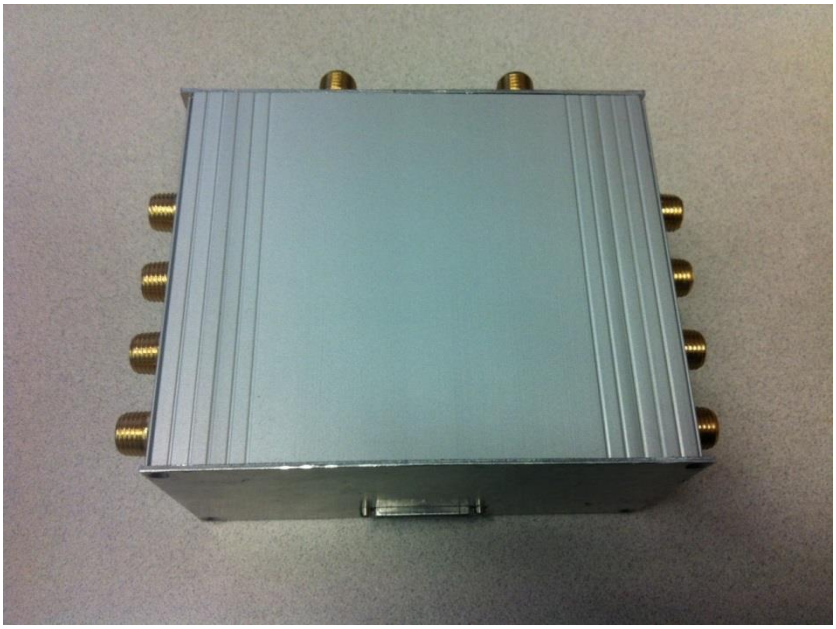

Figure 4. 19: The aluminum enclosure for interface board

4.4.3 Evaluation

The experiment was performed to evaluate the function of the interface PCB board. The test system contains controller box, VHDCI connector, Cartesian stage and interface board. The LED and photodiode fibers were placed parallel at the end of Cartesian stage. The interface board was connected to the black controller box through VHDCI connector as shown in Fig.4.20. The distance between the fibers ports and stage white label was adjusted. When the stage white label covered the fibers ports, the end of controller box shows 0 to 1, which is suitable jumping signal for motors.

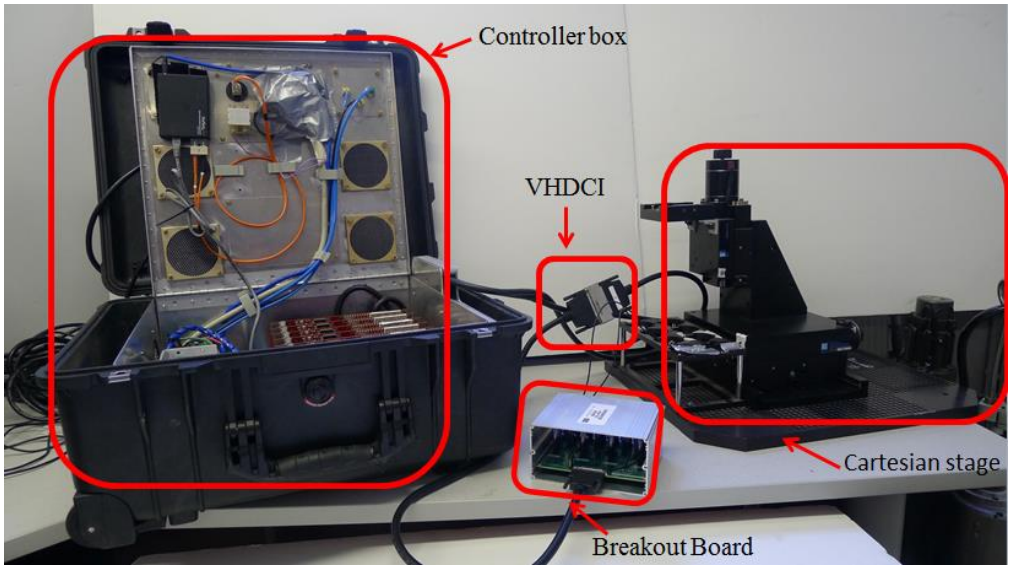

Figure 4. 20: General diagram of interface board evaluation

Another step is to adjust the vertical distance (shown is Fig.4.3) between the fibers ports and stage white label. The stable vertical distance ranges from 3.5mm to 6.5mm.

4.5 Conclusion

In this chapter, an interface board for PiezoBoard was designed to achieve eight channel optical limit switches, four channel motors and encoder connectors and four external master's encoders plugging in. The circuit was successfully connected and tested in breadboard. Furthermore, the PCB board was designed using Altium Designer and assembled in the aluminum enclosure. Finally, the interface board was integrated in control system and tested in lab environment.

5. Conclusion and Future Work

5.1 Conclusion

This thesis has covered many aspects involved in developing a MRI-Guided surgical robot including device mechanical design, driver system electronic design, system implementation and system evaluation and test. The thesis firstly gives a background of image-guided surgery and needle-based percutaneous intervention. The goal is to present and evaluate a MRI-compatible modular needle driver system for percutaneous interventions of prostate. The modular needle driver can stand on different kinds of base robots. This mechanical design could also be implemented on other base robots for some other standard percutaneous interventions, such as brain tumor.

At the beginning of this thesis, a reconfigurable MRI-guided modular needle driver is designed to support various needle-based interventions, such as straight needle insertion, asymmetric tip-based needle steering, and concentric-tube needle deployment. Each individual actuation unit can drive a single needle, tube, or cannula, and has 2 DOF motion, with 1 DOF linear translation and 1 DOF axial rotation. A cylindrical helix imaging coordinate registration fiducial frame is integrated in this needle driver to register the robot coordinate system to the patient coordinate system in MR image space. This fiducial frame is attached concentrically with the axis of the first actuation unit such that it translates and rotate with the needle or tube synchronously, which can achieve real-time tracking. The evaluation shows that the overall dimension of the needle driver set are 300x116x96mm. Each actuation unit can offer a 130mm linear translation and 360 degrees axial rotation. The RMS accuracy for the individual joints is 0.18mm (SD = 0.17mm).

Furthermore, a hardware controller system is introduced and improved for close loop control of the ultrasonic Shinsei motor integrated in base robot. A general schematic of generating two high voltage waveforms is introduced in this thesis. A transformer PCB board is designed to cooperate with piezoboard to achieve motion of base robot movement. It is demonstrated that the whole controller system directly drive the ultrasonic Shinsei motor forward and backward as well as velocity changing. An interface board is also designed and implemented to connect controller box and base robot, providing eight-channel optical limit switch, four motor and encoder connectors and four external encoder connectors. This interface board has been tested in the lab environment that it can immediately stop the Shinsei motor when the leg moves out of its range.

5.2 Future Work

One future aspect that needs to be done is to test the MRI-compatible modular needle driver in MR space using MRI-compatible piezoelectric motors. Eventually, this needle driver needs to be implemented in MRI space to achieve biopsy and brachytherapy for prostate cancer. An evaluation test in MRI environment could be performed in the future. This test could utilize the piezoelectric motor control box to steering the needle or tube in real gelatin, which is similar to tissue. Then the MR image of both gelatin and fiducial frame could be stored and sent to Matlab. Finally an algorithm could be used to complete the imaging processing and evaluate this mechanical design accuracy.

Another problem is the cooling of the MRI-compatible hardware control system. During the experiment, at least two pizeoboards and one transformer board were needed to plug in the backplane board. When the control system was powered, the pizeoboards produced lots of

heat, making it impossible to achieve long time working. With too much heat in the pizeoboard, the waveform synthesizer would generate unstable sin waveforms, and would prevent the ultrasonic motor from working normally. Two approaches have been attempted to solve this overheat problems. One is keeping air blowing near the overheated amplifiers and the other one is attaching a heat-conducting aluminum block. It was shown that both of two methods could cool this system just in short term. Therefore, more efficient cooling approaches should be developed and implemented in the MRI-compatible control system to guarantee the constant operating of ultrasonic motor.

Recently, the concept of concentric-tube robot has been proved to be feasible in [46][47][48]. More and more researchers consider it as the next generation tools of minimally invasive surgery because of its dexterity. The concentric-tube robot consists of several pre-curved needles or tubes and translates and rotates two continuum tubes to achieve complex 3D shapes. The reconfigurable needle driver can be used for the concentric-tube application because of its modularity design. With several actuation units placed along the lead screw and linear guide, this needle driver is able to offer more that 4-DOF needle placement mechanism and enables complex controlled motion.

Reference

[1] Das, J. Rucker, D.C. and Webster, R.J., 2010, “A Testbed for Multi-Lumen Steerable Needle Experiments”, Design of Medical Devices Conference, 2010.

[2] Comber, D.B., Cardona, D, Webster, R.J., and Barth, E.J., 2012, “Precision Pneumatic Robot for MRI-Guided Neurosurgery”, Design of Medical Devices Conference, 2012.

[3] Bedell, C., Lock, J., Gosline, A. and Dupont, P.E., 2011, “Design Optimization of Concentric Tube Robots Based on Task and Anatomical Constraints”, ICRA, 2011.

[4] Bruns, T.L, Tucke, J.M., Rucker, D.C., Swaney, P.J., and Webster, R.J., 2011, “Design of An Autoclavable Active Cannula Depoment Device”, Design of Medical Devices Conference, 2011.

[5] R. Galloway and T. Peters, “Overview and history of image-guided interventions," in Image-Guided Interventions (T. Peters and K. Cleary, eds.), pp. 1-21, Springer US, 2008

[6] T. Wang, C. Tang, and D. Liu, “A hybrid robot system guided by computer tomography for percutaneous lung cancer cryosurgery," Advanced Robotics, vol. 23, no. 10, pp. 1411-1422, 2009.

[7] C. Kim, F. Schafer, D. Chang, D. Petrisor, M. Han, and D. Stoianovici, “Robot for ultrasound-guided prostate imaging and intervention," in Intelligent Robots and Systems (IROS), 2011 IEEE/RSJ International Conference on, pp. 943-948, 2011.

[8] Krieger, R. Susil, C. Menard, J. Coleman, G. Fichtinger, E. Atalar, and L. Whitcomb, “Design of a novel MRI compatible manipulator for image guided prostate interventions," Biomedical Engineering, IEEE Transactions on, vol. 52, no. 2, pp. 306-313, 2005.

[9] Krieger, S.-E. Song, N. Cho, I. Iordachita, P. Guion, G. Fichtinger, and L. Whitcomb, “Development and evaluation of an actuated mri-compatible robotic system for MRI-guided prostate intervention," Mechatronics, IEEE/ASME Transactions on, vol. 18, no. 1, pp. 273-284, 2013.

[10]J. Cepek, B. Chronik, U. Lindner, J. Trachtenberg, and A. Fenster, “Development of an MRI-compatible device for prostate focal therapy," in Medical Image Computing and Computer-Assisted Intervention MICCAI 2012(N. Ayache, H. Delingette, P. Gol- land, and K. Mori, eds.), vol. 7510 of Lecture Notes in Computer Science, pp. 455-462, Springer Berlin Heidelberg, 2012.

[11]J. Cepek, B. Chronik, U. Lindner, J. Trachtenberg, and A. Fenster, “Development of an MRI-compatible device for prostate focal therapy," in Medical Image Computing and Computer-Assisted Intervention MICCAI 2012(N. Ayache, H. Delingette, P. Golland,

and K. Mori, eds.), vol. 7510 of Lecture Notes in Computer Science, pp. 455-462, Springer Berlin Heidelberg, 2012.

[12]H. Elhawary, Z. Tse, M. Rea, A. Zivanovic, null, C. Besant, N. de Souza, D. McRobbie, I. Young, and M. Lamperth, "Robotic system for transrectal biopsy of the prostate: Real-time guidance under MRI," Engineering in Medicine and Biology Magazine, IEEE, vol. 29, no. 2, pp. 78-86, 2010.

[13]S.-E. Song, N. Cho, G. Fischer, N. Hata, C. Tempany, G. Fichtinger, and I. Iordachita, "Development of a pneumatic robot for MRI-guided transperineal prostate biopsy and brachytherapy: New approaches," in Robotics and Automation (ICRA), 2010 IEEE International Conference on, pp. 2580-2585, 2010.

[14]Li G, Su H, Shang W, Tokuda J, Hata N, Tempany CM, Fischer GS, A Fully Actuated Robotic Assistant for MRI-Guided Prostate Biopsy and Brachytherapy, SPIE Medical Imaging (Image-Guided Procedures, Robotic Interventions, and Modeling Conference), Orlando, USA, Feb. 2013. SPIE

[15]Y. Yu, T. Podder, Y. Zhang, W.-S. Ng, V. Misic, J. Sherman, L. Fu, D. Fuller, E. Messing, D. Rubens, J. Strang, and R. Brasacchio, "Robot-assisted prostate brachytherapy," in Medical Image Computing and Computer-Assisted Intervention MICCAI 2006 (R. Larsen, M. Nielsen, and J. Sporring, eds.), vol. 4190 of Lecture Notes in Computer Science, pp. 41-49, Springer Berlin Heidelberg, 2006.

[16]G. Fichtinger, T. L. DeWeese, A. Patriciu, A. Tanacs, D. Mazilu, J. H. Anderson, K. Masamune, R. H. Taylor, and D. Stoianovici, "System for robotically assisted prostate biopsy and therapy with intraoperative ct guidance," Academic Radiology, vol. 9, no. 1, pp. 60-74, 2002.

[17]http://www.cancer.org/cancer/prostatecancer/detailedguide/prostate-cancer-key-statistics

[18]Su H, Camilo A, Cole GA, Tempany CM, Hata N, Fischer GS, High-Field MRI-Compatible Needle Placement Robot for Prostate Interventions, Proceedings of MMVR18 (Medicine Meets Virtual Reality), Newport Beach, California, USA, February, 2011

[19]Su H., Zervas M., Cole G.A., Furlong C., Fischer G.S., "Real-time MRI-Guided Needle Placement Robot with Integrated Fiber Optic Force Sensing," International Conference on Robotics and Automation, Shanghai, China, pp 1583-1588 (2011)

[20]Cole, G., Pilitsis, J. and Fischer, G. S., "Design of a Robotic System for MRI-Guided Deep Brain Stimulation Electrode Placement," International Conference on Robotics and Automation - ICRA 2009, Kobe, Japan, 4450-4456 (2009)

[21]U. Lindner, A. Goldenberg, M. A. Haider, W. Kucharczyk, R. A. Weersink, M. Sussman, Y. Yi, L. Ma, and J. Trachtenberg, "Robot-assisted mri-guided prostatic interventions," The Journal of Urology, vol. 181, no. 4, Supplement, pp. 319 , 2009.

[22]Krieger, A., Iordachita, I.I., Gu ion, P., Singh, A.K., Kaushal, A., Menard, C., Pinto, P.A., Camphausen, K., Fichtinger, G., Whitcomb, L.L., "An MRI-Compatible Robotic System With Hybrid Tracking for MRI-Guided Prostate Intervention," IEEE Transactions on Biomedical Engineering, vol.58, no.11, pp.3049-3060 (2011)

[23]Derbyshire, J. A., Wright, G. A., Henkelmann, R. M. and Hinks, S., "Dynamic scan-plane tracking using MR positioning monitoring," J. Magn. Reson. Imaging, 8, 924 –932 (1998)

[24]Hillenbrand, C. M., Elgort, D. R., Wong, E. D., Reykowski, A., Wacker, F. K., Lewin, J. S. and Duerk, J. L., "Active device tracking and high-resolu tion intravascular MRI using a novel catheter-based, opposed-solenoid phased array coil," Magn. Reson. Med., 51, 668– 75 (2004)

[25]DiMaio, S., Samset, E., Fischer, G.S., Iordachita, I., Fichtinger, G., Jolesz, F. and Tempany, C., "Dynamic MRI Scan Plane Control for Passive Tracking of Instruments and Devices" MICCAI 2007, LNCS, vol. 4792, 50–58, Springer, Heidelberg (2007)

[26]Susil, R. C., Anderson, J.H. and Taylor, R.H., "A Single Image Registration Method for CT Guided Interventions," MICCAI 1999, Cambridge, England, LNCS 1679, 798-808 (1999)

[27]Lee, S., Fichtinger, G. and Chirikjian, G.S., "Numerical algorithms for spatial registration of line fiducials from cross-sectional images," Med. Phys., vol. 29, 1881–1891 (2002)

[28]Shang, W. and Fischer, G. S., "A High Accuracy Multi-Image Registration Method for Tracking MRI-Guided Robots," SPIE Medical Imaging, Image-Guided Procedures, Robotic Interventions, and Modeling Conference (2012)

[29]Y. Ma, I. Dobrev, W. Shang, H. Su, S. Janga, and G. Fischer, "Chic: Cylindrical helix imaging coordinate registration fiducial for MRI-guided interventions," in Engineering in Medicine and Biology Society (EMBC), 2012 Annual International Conference of the IEEE, pp. 2808-2812, 2012.

[30]Wang, Y., Cole, G.A., Su, H., Pilitsis, J.G., and Fischer, G.S, 2009, "MRI Compatibility Evaluation of a Piezoelectric Actuator System for a Neural Interventional Robot", 31st Annual International Conference of the IEEE EMBS, 2009.

[31]Piezo LEGS Rotary 80mNm. http://www.piezomotor.se/documents/150060_LR80.pdf

[32]EM1 Transmissive Optical Encoder Module. http://www.usdigital.com/assets/datasheets/EM1_datasheet.pdf?k=635009540424168038

[33]DCM-21x3 Ethernet/RS232 Econo Motion Controllers, 1-8 axes. http://www.galilmc.com/catalog/cat21x2x3.pdf

[34]DMC-21x3 Amplifiers & Accessories. http://www.galilmc.com/support/manuals/21x3_accessories.pdf

[35]http://www.seminarsonly.com/Labels/Ultrasonic-Motor-Abstract.php

[36]B. Radi and A. E. Hami, "The study of the dynamic contact in ultrasonic motor," Applied Mathematical Modelling, vol. 34, no. 12, pp. 3767-3777, 2010.

[37]http://www.technohands.co.jp/en/products/um-pumr.html

[38]Ultrasonic Motor. http://wenku.baidu.com/view/3346f7dfa58da0116c17496b.html

[39]G. Cole, K. Harrington, H. Su, A. Camilo, J. Pilitsis, and G. Fischer, "Closed-loop actuated surgical system utilizing real-time in situ MRI guidance," in 12th International Symposium on Experimental Robotics - ISER 2010, New Delhi and Agra, India, Dec. 2010.

[40]http://upload.wikimedia.org/wikipedia/commons/6/64/Transformer3d_col3.svg

[41]IF-E91A Plastic Fiber Optical IR LEDS. http://i-fiberoptics.com/pdf/ife91a.pdf

[42]IF-D91 Plastic Fiber Optic Photodiode. http://i-fiberoptics.com/pdf/ifd91.pdf

[43]http://www.lpi.usra.edu/education/fieldtrips/2005/activities/ir_spectrum/images/emspectrum.jpg

[44]Precision, Low Noise, CMOS, Rail-to-Rail, Input/Output Operational Amplifiers AD8606. http://www.analog.com/static/imported-files/data_sheets/AD8605_8606_8608.pdf

[45]AM26C31C, AM26C31I, AM26C31M QUADRUPLE DIFFERENTIAL LINE DRIVERS. http://www.datasheetcatalog.org/datasheets2/15/154340_1.pdf

[46]P. Dupont, J. Lock, B. Itkowitz, and E. Butler, "Design and control of concentric-tube robots" Robotics, IEEE Transactions on, vol. 26, no. 2, pp. 209-225, 2010.

[47]D. Rucker, B. Jones, and R. Webster, "A geometrically exact model for externally loaded concentric-tube continuum robots." Robotics, IEEE Transactions on, vol. 26, no. 5, pp. 769-780, 2010.

[48]H. Su, D. Cardona, W. Shang, A. Camilo, G. Cole, D. Rucker, R. Webster, and G. Fischer, “A MRI-guided concentric tube continuum robot with piezoelectric actuation: A feasibility study," in Robotics and Automation (ICRA), 2012 IEEE International Conference on, pp. 1939-1945, 2012.

Vita

Wenzhi Ji was born on September 13, 1988 in Yancheng, Jiangsu, China. He received the B.E. degree in Biomedical Engineering from Nanjing University of Aeronautics and Astronautics in 2011 and enrolled in the Biomedical Engineering graduate program at Worcester Polytechnic Institute (WPI) in 2013. Since 2012, he has been in Automation and Interventional Medicine (AIM) Robotics Research Laboratory in WPI. His research interests focus on development of MRI-compatible robotic systems including medical robot mechanism design, MRI-compatible actuation techniques and electronic design.